

Department of Mathematics and Statistics

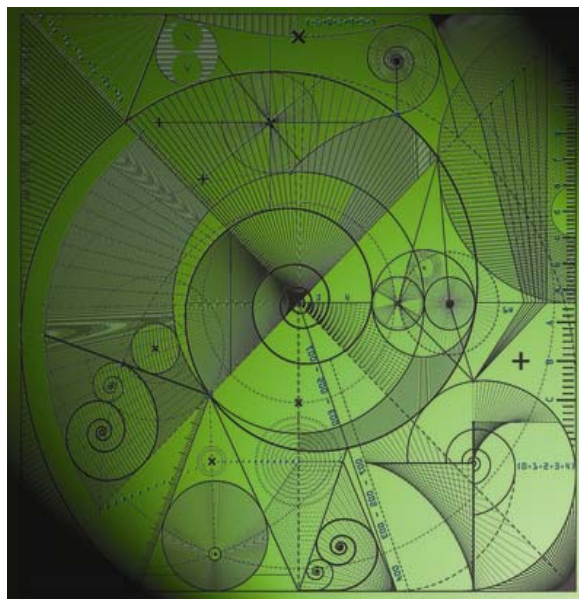
Preprint MPS-2012-02

13 February 2012

The Unsteady Flow of a Weakly Compressible Fluid in a Thin Porous Layer III: Three-dimensional Computations

by

S. Langdon, D.J. Needham, B.A. Samson
and J.P. Gilchrist



THE UNSTEADY FLOW OF A WEAKLY COMPRESSIBLE FLUID IN A THIN POROUS LAYER III: THREE-DIMENSIONAL COMPUTATIONS

by S. LANGDON

*(Department of Mathematics and Statistics, University of Reading,
Reading RG6 6AX, UK)*

D. J. NEEDHAM

*(School of Mathematics, University of Birmingham,
Birmingham B15 2TT, UK)*

B. A. SAMSON and J. P. GILCHRIST

(Schlumberger Oilfield UK Plc, Wyndyke Furlong, Abingdon OX14 1UJ, UK)

Summary

We describe a novel method for determining the pressure and velocity fields for a weakly compressible fluid flowing in a thin three-dimensional layer composed of an inhomogeneous, anisotropic porous medium, with vertical side walls and variable upper and lower boundaries, in the presence of vertical wells injecting and/or extracting fluid. Our approach uses the method of matched asymptotic expansions to derive expressions for all significant process quantities, the computation of which requires only the solution of linear, elliptic, two-dimensional boundary-value and eigenvalue problems. In this paper we provide full implementation details and present numerical results demonstrating the efficiency and accuracy of our scheme.

1. Introduction

A problem with significant applications in the oil and gas industry, and also to water resource management, is that of computing the pressure and velocity fields for a weakly compressible fluid flowing in a porous medium, with wells injecting or extracting fluid considered as line sources and sinks respectively. The (in general) heterogeneity of the porous medium, compressibility of the fluid, singularities induced by the source and sink terms, large size of the computational domain and long time interval over which simulations are often required make accurate and efficient modelling of such a scenario an extremely challenging task. Problems such as this have been very widely considered in the literature; we refer to e.g. (1, 2) and the many references therein for a detailed summary of the modelling and computational issues that must be resolved.

Here, we consider the case of fluid flowing in a porous three-dimensional (3-d) layer of inhomogeneous and anisotropic permeability, with variable upper and lower boundaries and vertical side walls and wells. Numerical solution of the full equations of motion throughout the layer can be prohibitively expensive. The approach we present in this paper is based on the key observation that in geophysical applications the depth scale h of the layer is often small compared to the length scale l . For example, in (3) numerical results for single-phase

flow in 3-d compressible porous media in the presence of multiple line sources and sinks are presented for examples with $h/l \approx 1/40$; results in (4), for single-phase fluid flow in two-dimensional (2-d) axisymmetric and anisotropic porous media, are presented for examples with $h/l \approx 1/500$.

Whereas for standard numerical schemes this small aspect ratio can be problematical, here we present an approach based on matched asymptotic expansions in $\epsilon \sim h/l \ll 1$ (defined explicitly in (2.10) below) for which the accuracy improves as $\epsilon \rightarrow 0$. These ideas were first proposed in (5), for the 2-d problem, and subsequently extended to the full 3-d problem that we consider here in (6). The work in (6) consists of a rigorous derivation of the matched asymptotic expansions, leading to expressions for the pressure and velocity fields throughout the layer accurate to $O(\epsilon^2)$. Determining the actual values of the leading order terms in these asymptotic expansions requires the solution of linear, elliptic boundary-value and eigenvalue problems on the 2-d projection of the layer cross-section. Here, we consider the implementation of the scheme proposed in (6). We begin in §2 by describing the initial-boundary value problem that we wish to solve and presenting the ideas of (6) in an algorithmic fashion. In §3 we give full computational details for the solution of the resulting 2-d problems and explain how to combine the different components of the solution in order to achieve numerical values for the pressure and velocity fields throughout the layer. We present numerical results demonstrating the exceptional efficiency of our approach in §4, and finally in §5 we draw some conclusions.

Unlike fully numerical schemes, the accuracy of our approach is limited by the value of ϵ . Provided ϵ is small however, our approach is shown to replicate anticipated qualitative features of the solution in a fraction of the time that would be required by fully numerical solvers. Our approach requires no temporal discretisation, and the pressure and velocity fields can be obtained over any interval of time with constant production rates with virtually the same cost as computing them at a single time. The only spatial discretisation required is on the 2-d projection of the layer cross-section and on the one-dimensional (1-d) vertical line sources and sinks. Moreover, changes to production rates and well locations can be easily accounted for, as can changes to porosity and permeability of the layer. The latter feature might make this approach particularly well suited to history matching applications (see, e.g., the discussions in (7, 8)).

2. The initial-boundary value problem, and its solution via matched asymptotic expansions

As in (6) we consider the flow of a weakly compressible fluid in the presence of vertical line sources and sinks, in a 3-d reservoir of porous medium with variable upper and lower boundary. The reservoir has permeability which is both inhomogeneous and anisotropic. We adopt the same notation as in (6), and refer to (6, §2) for the derivation of the dimensionless equations of motion,

$$\bar{\phi}(x, y, z) \frac{\partial \bar{p}}{\partial t} + \frac{\partial u}{\partial x} + \frac{\partial v}{\partial y} + \frac{\partial w}{\partial z} = \sum_{i=1}^N s_i(z) \delta(x - x_i) \delta(y - y_i), \quad (2.1)$$

$$u = -D_x(x, y, z) \frac{\partial \bar{p}}{\partial x}, \quad (2.2)$$

$$v = -D_y(x, y, z) \frac{\partial \bar{p}}{\partial y}, \quad (2.3)$$

$$\epsilon^2 w = -D_z(x, y, z) \frac{\partial \bar{p}}{\partial z}, \quad (2.4)$$

for $(x, y, z) \in M'$, $t \in (0, \infty)$, whose solution we will study in this paper. Here (x, y, z) are rectangular cartesian coordinates with z pointing vertically upwards, and the dimensionless domain is

$$M' = \{(x, y, z) \in \mathbb{R}^3 : (x, y) \in \Omega, z \in (z_-(x, y), z_+(x, y))\}, \quad (2.5)$$

with closure $\overline{M'}$ and boundary $\partial M'$, where $\Omega \subset \mathbb{R}^2$ is bounded by the simple closed piecewise smooth curve $\partial\Omega \subset \mathbb{R}^2$, with $\overline{\Omega} = \Omega \cup \partial\Omega$, and $z_+, z_- : \overline{\Omega} \mapsto \mathbb{R}$ are such that $z_+, z_- \in C^1(\overline{\Omega})$, and $z_+(x, y) > z_-(x, y)$ for all $(x, y) \in \overline{\Omega}$. In (2.1)–(2.4), \bar{p} is the dynamic fluid pressure, with the pressure field given by

$$p(x, y, z, t) = -\hat{\sigma}z + \bar{p}(x, y, z, t), \quad (2.6)$$

where $\hat{\sigma}$ is a dimensionless parameter, u, v and w are the components of the fluid velocity field in the x, y and z directions respectively, and $\bar{\phi} \in C^1(\overline{M'})$ denotes the porosity of the layer, bounded above zero on $\overline{M'}$ and scaled so that

$$\iiint_{M'} \bar{\phi}(x, y, z) dx dy dz = \text{meas}(\overline{M}), \quad (2.7)$$

with $\text{meas}(\overline{M'}) = \iint_{\Omega} z_+(x, y) - z_-(x, y) dx dy$, being the measure (volume) of $\overline{M'} \subset \mathbb{R}^3$. The line source/sink locations are at $(x_i, y_i) \in \Omega$, $i = 1, \dots, N$. The functions $s_i : [z_-(x_i, y_i), z_+(x_i, y_i)] \mapsto \mathbb{R}$, $i = 1, \dots, N$, represent the line source/sink volumetric strengths, with $s_i \in C([z_-(x_i, y_i), z_+(x_i, y_i)])$, $i = 1, \dots, N$. The dimensionless total volume flux from the i^{th} line source/sink is then,

$$\alpha_i = \frac{1}{Q} \int_{z_-(x_i, y_i)}^{z_+(x_i, y_i)} s_i(\mu) d\mu, \quad i = 1, \dots, N, \quad (2.8)$$

where

$$Q = \sum_{i=1}^N \left| \int_{z_-(x_i, y_i)}^{z_+(x_i, y_i)} s_i(\lambda) d\lambda \right|, \quad (2.9)$$

and the scaling of α_i by $1/Q$ ensures that $|\alpha_i| \leq 1$, for $i = 1, \dots, N$, and $\sum_{i=1}^N |\alpha_i| = 1$. In (2.1) $\delta : \mathbb{R} \mapsto \mathbb{R}$ is the usual Dirac delta function. The functions $D_x, D_y, D_z : \overline{M'} \mapsto \mathbb{R}^+$ in (2.2)–(2.4) represent the variable permeabilities in the x, y and z directions respectively, and are such that $D_x, D_y, D_z \in C^1(\overline{M'})$ and are bounded above zero on $\overline{M'}$. Finally, the dimensionless parameter $\epsilon \ll 1$ is given by

$$\epsilon = \sqrt{\frac{D_0^H h}{D_0^L l}}, \quad (2.10)$$

where $l > 0$ is the horizontal length scale of the dimensional reservoir, $h > 0$ is the vertical length scale associated with the dimensional reservoir, and $D_0^H, D_0^L > 0$ are

permeability scales (divided by constant fluid velocity) in the horizontal and vertical directions respectively. Our matched asymptotic approach will rely on the assumption that $\epsilon \ll 1$. This is often the case in practice, with oil and gas reservoirs typically extending many orders of magnitude further horizontally compared to their depth.

The boundary conditions are, in dimensionless form,

$$(u(\mathbf{r}, t), v(\mathbf{r}, t), w(\mathbf{r}, t)) \cdot \hat{\mathbf{n}} = 0, \quad \text{for all } (\mathbf{r}, t) \in \partial M'_H \times (0, \infty), \quad (2.11)$$

$$w(\mathbf{r}, t) - \left\{ \frac{\partial z_+}{\partial x}(x, y)u(\mathbf{r}, t) + \frac{\partial z_+}{\partial y}(x, y)v(\mathbf{r}, t) \right\} = 0, \quad \text{for all } (\mathbf{r}, t) \in \partial M'_+ \times (0, \infty), \quad (2.12)$$

$$w(\mathbf{r}, t) - \left\{ \frac{\partial z_-}{\partial x}(x, y)u(\mathbf{r}, t) + \frac{\partial z_-}{\partial y}(x, y)v(\mathbf{r}, t) \right\} = 0, \quad \text{for all } (\mathbf{r}, t) \in \partial M'_- \times (0, \infty), \quad (2.13)$$

where $\hat{\mathbf{n}}(x, y)$ for $(x, y) \in \partial\Omega$ represents the outward unit normal field to $\partial\Omega$, $\partial M'_H \subset \partial M'$ is that part of $\partial M'$ representing the side walls of the boundary, $\partial M'_+, \partial M'_- \subset \partial M'$ represent the upper and lower surfaces of $\partial M'$ respectively, with $\partial M'_+ \cup \partial M'_- \cup \partial M'_H = \partial M'$, and $\mathbf{r} := (x, y, z)$. Finally we have the initial condition,

$$\bar{p}(\mathbf{r}, 0) = \bar{p}_0 f(\mathbf{r}), \quad \text{for all } \mathbf{r} \in \bar{M}', \quad (2.14)$$

with \bar{p}_0 the reference pressure for the weakly compressible fluid, and $f : \bar{M}' \mapsto \mathbb{R}$ the prescribed initial pressure variation, with

$$f \in PC^1(\bar{M}') \cap C(\bar{M}'), \quad (2.15)$$

where $PC^1(\bar{M}')$ represents the class of piecewise continuously differentiable functions on \bar{M}' . The full problem for consideration is then given by (2.1)–(2.4), (2.11)–(2.14), which we refer to henceforth as [IBVP].

Direct solution of the linear inhomogeneous parabolic problem [IBVP] is problematical, not least due to the inhomogeneous right hand side and the singularities in the solutions at the source/sink locations. To simplify the problem, we decompose it into two easier problems: a pseudo-steady state problem (denoted by [PSSP]), which is an elliptic weighted Neumann problem with an inhomogeneous right hand side and identical similarities to [IBVP] but with the time dependence removed, and a transient problem, a linear homogeneous parabolic problem with the singularities removed, whose solution reduces to the solution of a regular self adjoint eigenvalue problem (denoted by [EVP]). Specifically, it follows from (6, Theorem 2.2) that for each $\epsilon > 0$, [IBVP] has a unique solution $u, v, w, \bar{p} : \bar{M}' \times [0, \infty) \mapsto \mathbb{R}$ that we can write as

$$\bar{p}(\mathbf{r}, t) = \hat{\alpha}_T t + \hat{p}(\mathbf{r}) + \tilde{p}(\mathbf{r}, t), \quad (2.16)$$

$$u(\mathbf{r}, t) = \hat{u}(\mathbf{r}) - D_x(\mathbf{r}) \frac{\partial \tilde{p}}{\partial x}(\mathbf{r}, t), \quad (2.17)$$

$$v(\mathbf{r}, t) = \hat{v}(\mathbf{r}) - D_y(\mathbf{r}) \frac{\partial \tilde{p}}{\partial y}(\mathbf{r}, t), \quad (2.18)$$

$$w(\mathbf{r}, t) = \hat{w}(\mathbf{r}) - \epsilon^{-2} D_z(\mathbf{r}) \frac{\partial \tilde{p}}{\partial z}(\mathbf{r}, t), \quad (2.19)$$

for all $(\mathbf{r}, t) \in \overline{M}' \times [0, \infty)$, where the constant $\hat{\alpha}_T$, representing the weighted dimensionless net flux of fluid into or out of the porous layer, is given by

$$\hat{\alpha}_T = \frac{1}{\text{meas}(\overline{M}')} \sum_{i=1}^N \alpha_i. \quad (2.20)$$

Here $\hat{u}, \hat{v}, \hat{w}, \hat{p} : \overline{M}' \mapsto \mathbb{R}$ is the unique solution to the pseudo-steady state problem [PSSP]:

$$\frac{\partial \hat{u}}{\partial x} + \frac{\partial \hat{v}}{\partial y} + \frac{\partial \hat{w}}{\partial z} = \sum_{i=1}^N s_i(z) \delta(x - x_i) \delta(y - y_i) - \hat{\alpha}_T \bar{\phi}(x, y, z), \quad (x, y, z) \in M', \quad (2.21)$$

$$\hat{u} = -D_x(x, y, z) \frac{\partial \hat{p}}{\partial x}, \quad \hat{v} = -D_y(x, y, z) \frac{\partial \hat{p}}{\partial y}, \quad \epsilon^2 \hat{w} = -D_z(x, y, z) \frac{\partial \hat{p}}{\partial z}, \quad (x, y, z) \in M', \quad (2.22)$$

$$(\hat{u}(\mathbf{r}), \hat{v}(\mathbf{r}), \hat{w}(\mathbf{r})) \cdot \hat{\mathbf{n}} = 0, \quad \text{for all } \mathbf{r} \in \partial M'_H, \quad (2.23)$$

$$\hat{w}(\mathbf{r}) - \left\{ \frac{\partial z_+}{\partial x}(x, y) \hat{u}(\mathbf{r}) + \frac{\partial z_+}{\partial y}(x, y) \hat{v}(\mathbf{r}) \right\} = 0, \quad \text{for all } \mathbf{r} \in \partial M'_+, \quad (2.24)$$

$$\hat{w}(\mathbf{r}) - \left\{ \frac{\partial z_-}{\partial x}(x, y) \hat{u}(\mathbf{r}) + \frac{\partial z_-}{\partial y}(x, y) \hat{v}(\mathbf{r}) \right\} = 0, \quad \text{for all } \mathbf{r} \in \partial M'_-, \quad (2.25)$$

accompanied by the constraint (to enforce uniqueness)

$$\iiint_{M'} \hat{p}(x, y, z) \bar{\phi}(x, y, z) \, dx \, dy \, dz = \iiint_{M'} \bar{p}_0 f(x, y, z) \bar{\phi}(x, y, z) \, dx \, dy \, dz =: I_0. \quad (2.26)$$

The transient pressure field $\tilde{p} : \overline{M}' \times [0, \infty) \mapsto \mathbb{R}$ satisfies the following linear, strongly parabolic, regular, initial-boundary value problem:

$$\bar{\phi}(x, y, z) \frac{\partial \tilde{p}}{\partial t} - \left\{ \frac{\partial}{\partial x} \left(D_x(x, y, z) \frac{\partial \tilde{p}}{\partial x} \right) + \frac{\partial}{\partial y} \left(D_y(x, y, z) \frac{\partial \tilde{p}}{\partial y} \right) + \frac{\partial}{\partial z} \left(\epsilon^{-2} D_z(x, y, z) \frac{\partial \tilde{p}}{\partial z} \right) \right\} = 0, \quad (2.27)$$

$$[\tilde{D}(\mathbf{r}) \nabla \tilde{p}(\mathbf{r}, t)] \cdot \hat{\mathbf{n}} = 0, \quad \text{for all } (\mathbf{r}, t) \in \partial M'_H \times (0, \infty), \quad (2.28)$$

$$[\tilde{D}(\mathbf{r}) \nabla \tilde{p}(\mathbf{r}, t)] \cdot \left(-\epsilon^2 \frac{\partial z_+}{\partial x}(x, y), -\epsilon^2 \frac{\partial z_+}{\partial y}(x, y), 1 \right) = 0, \quad (2.29)$$

$$\text{for all } (\mathbf{r}, t) \in \partial M'_+ \times (0, \infty),$$

$$[\tilde{D}(\mathbf{r}) \nabla \tilde{p}(\mathbf{r}, t)] \cdot \left(-\epsilon^2 \frac{\partial z_-}{\partial x}(x, y), -\epsilon^2 \frac{\partial z_-}{\partial y}(x, y), 1 \right) = 0, \quad (2.30)$$

$$\text{for all } (\mathbf{r}, t) \in \partial M'_- \times (0, \infty),$$

$$\tilde{p}(\mathbf{r}, 0) = \bar{p}_0 f(\mathbf{r}) - \hat{p}(\mathbf{r}) = \tilde{p}_0(\mathbf{r}), \quad \text{for all } \mathbf{r} \in \overline{M}'. \quad (2.31)$$

Here

$$\tilde{D}(\mathbf{r}) = \begin{pmatrix} -D_x(x, y, z) & 0 & 0 \\ 0 & -D_y(x, y, z) & 0 \\ 0 & 0 & -D_z(x, y, z) \end{pmatrix},$$

for all $\mathbf{r} \in \overline{M}'$. It follows from (2.26) that $\tilde{p}_0(\mathbf{r})$ satisfies

$$\iiint_{M'} \tilde{p}_0(x, y, z) \bar{\phi}(x, y, z) dx dy dz = 0. \quad (2.32)$$

The transient velocity fields $\tilde{u} = u - \hat{u}$, $\tilde{v} = v - \hat{v}$, $\tilde{w} = w - \hat{w}$ are then given by

$$\tilde{u} = -D_x(x, y, z) \frac{\partial \tilde{p}}{\partial x}, \quad \tilde{v} = -D_y(x, y, z) \frac{\partial \tilde{p}}{\partial y}, \quad \epsilon^2 \tilde{w} = -D_z(x, y, z) \frac{\partial \tilde{p}}{\partial z}, \quad (\mathbf{r}, t) \in M' \times (0, \infty). \quad (2.33)$$

It is shown in (6) that the solution to (2.27)–(2.31) (together with an appropriate regularity condition, see (6) for details) is given by

$$\tilde{p}(\mathbf{r}, t) = \sum_{n=1}^{\infty} a_n(\epsilon) e^{-\lambda_n(\epsilon)t} \phi_n(\mathbf{r}; \epsilon), \quad \text{for all } (\mathbf{r}, t) \in \overline{M}' \times [0, \infty), \quad (2.34)$$

with $a_0(\epsilon) = 0$, via (2.32), and

$$a_j(\epsilon) = \iiint_{M'} \tilde{p}_0(x, y, z) \bar{\phi}(x, y, z) \phi_j(x, y, z; \epsilon) dx dy dz \quad (2.35)$$

for $j = 1, 2, \dots$, where $\lambda = \lambda_j(\epsilon) \in \mathbb{C}$ and $\phi = \phi_j : \overline{M}' \mapsto \mathbb{R}$, $j = 0, 1, 2, \dots$, are the eigenvalues and corresponding eigenfunctions of the self-adjoint eigenvalue problem in \overline{M}' ,

$$\frac{\partial}{\partial x} \left(D_x(x, y, z) \frac{\partial \phi}{\partial x} \right) + \frac{\partial}{\partial y} \left(D_y(x, y, z) \frac{\partial \phi}{\partial y} \right) + \frac{\partial}{\partial z} \left(\epsilon^{-2} D_z(x, y, z) \frac{\partial \phi}{\partial z} \right) + \lambda \bar{\phi}(x, y, z) \phi = 0,$$

for $(x, y, z) \in M'$,

$$[\tilde{D}(\mathbf{r}) \nabla \phi(\mathbf{r})] \cdot \hat{\mathbf{n}} = 0, \quad \text{for all } \mathbf{r} \in \partial M'_H,$$

$$[\tilde{D}(\mathbf{r}) \nabla \phi(\mathbf{r})] \cdot \left(-\epsilon^2 \frac{\partial z_+}{\partial x}(x, y), -\epsilon^2 \frac{\partial z_+}{\partial y}(x, y), 1 \right) = 0, \quad \text{for all } \mathbf{r} \in \partial M'_+,$$

$$[\tilde{D}(\mathbf{r}) \nabla \phi(\mathbf{r})] \cdot \left(-\epsilon^2 \frac{\partial z_-}{\partial x}(x, y), -\epsilon^2 \frac{\partial z_-}{\partial y}(x, y), 1 \right) = 0, \quad \text{for all } \mathbf{r} \in \partial M'_-,$$

which we denote by [EVP]. The eigenvalues and eigenfunctions satisfy (see (6))

$$0 = \lambda_0(\epsilon) < \lambda_1(\epsilon) \leq \lambda_2(\epsilon) \leq \dots, \quad (2.36)$$

$$\langle \phi_i, \phi_j \rangle = \iiint_{M'} \bar{\phi}(x, y, z) \phi_i(x, y, z; \epsilon) \phi_j(x, y, z; \epsilon) dx dy dz = \delta_{ij}, \quad \text{for } i, j = 0, 1, 2, \dots,$$

with δ_{ij} the Kronecker delta symbol and $\phi_0(x, y, z; \epsilon) = (\text{meas}(\overline{M}'))^{-1/2}$, for $(x, y, z) \in \overline{M}'$.

To complete the solution to [IBVP], we thus need to find $\hat{p}, \hat{u}, \hat{v}, \hat{w} : \overline{M}' \mapsto \mathbb{R}$ solving the pseudo-steady state problem [PSSP] (given by (2.21)–(2.26)), and $\lambda_n(\epsilon) (> 0)$ and its corresponding eigenfunction $\phi_n : \overline{M}' \mapsto \mathbb{R}$, for each $n = 1, 2, \dots$, solving the eigenvalue problem [EVP]. Under the assumption that $0 < \epsilon \ll 1$, we construct solutions to [PSSP] and [EVP] in the asymptotic limit $\epsilon \rightarrow 0$, via matched asymptotic expansions for the solutions of the equations of motion of the fluid both in the vicinity of each well (the *inner* region), and away from the wells (the *outer* region).

2.1 Solution to [PSSP]

It is shown in (6, §3) that the outer region asymptotic expansions (away from the sources/sinks) are given by

$$\hat{p}(\mathbf{r}; \epsilon) = A(x, y) + O(\epsilon^2), \quad (2.37)$$

$$\hat{u}(\mathbf{r}; \epsilon) = -D_x(x, y, z) \frac{\partial A}{\partial x}(x, y) + O(\epsilon^2), \quad (2.38)$$

$$\hat{v}(\mathbf{r}; \epsilon) = -D_y(x, y, z) \frac{\partial A}{\partial y}(x, y) + O(\epsilon^2), \quad (2.39)$$

$$\begin{aligned} \hat{w}(\mathbf{r}; \epsilon) = & \int_{z_-(x,y)}^z \left\{ \frac{\partial}{\partial x} \left(D_x(x, y, \xi) \frac{\partial A}{\partial x}(x, y) \right) + \frac{\partial}{\partial y} \left(D_y(x, y, \xi) \frac{\partial A}{\partial y}(x, y) \right) \right\} d\xi \\ & - \hat{\alpha}_T \int_{z_-(x,y)}^z \bar{\phi}(x, y, \xi) d\xi + O(\epsilon^2), \end{aligned} \quad (2.40)$$

as $\epsilon \rightarrow 0$, uniformly for $\mathbf{r} \in \bar{M}' \setminus \bigcup_{i=1}^N \delta_i^\epsilon$, where δ_i^ϵ is an $O(\epsilon)$ neighbourhood of \bar{d}_i , with

$$d_i = \{(x, y, z) \in \bar{M}' : (x, y) = (x_i, y_i), z \in (z_-(x_i, y_i), z_+(x_i, y_i))\},$$

for each $i = 1, \dots, N$, and $A : \bar{\Omega} \mapsto \mathbb{R}$ is the solution to the linear, inhomogeneous, strongly elliptic boundary value problem (which we will refer to henceforth as [BVP]),

$$\frac{\partial}{\partial x} \left(\bar{D}_x(x, y) \frac{\partial A}{\partial x}(x, y) \right) + \frac{\partial}{\partial y} \left(\bar{D}_y(x, y) \frac{\partial A}{\partial y}(x, y) \right) = F(x, y), \quad (x, y) \in \Omega, \quad (2.41)$$

$$\bar{D}_x(x, y) \frac{\partial A}{\partial x}(x, y) n_x(x, y) + \bar{D}_y(x, y) \frac{\partial A}{\partial y}(x, y) n_y(x, y) = 0, \quad (x, y) \in \partial\Omega, \quad (2.42)$$

$$\iint_{\Omega} \hat{\phi}(x, y) A(x, y) dx dy = I_0. \quad (2.43)$$

Here the right hand side of (2.41) is

$$F(x, y) := - \sum_{i=1}^N \alpha_i \delta(x - x_i) \delta(y - y_i) + \hat{\alpha}_T \hat{\phi}(x, y), \quad (x, y) \in \Omega,$$

the depth integrated permeability of the porous layer $\hat{\phi} : \bar{\Omega} \mapsto \mathbb{R}$ is given by

$$\hat{\phi}(x, y) = \int_{z_-(x,y)}^{z_+(x,y)} \bar{\phi}(x, y, \xi) d\xi, \quad \text{for } (x, y) \in \bar{\Omega},$$

and the depth integrated permeabilities of the porous layer in the x and y directions respectively, $\bar{D}_x, \bar{D}_y : \bar{\Omega} \mapsto \mathbb{R}$, are defined by

$$\bar{D}_x(x, y) = \int_{z_-(x,y)}^{z_+(x,y)} D_x(x, y, \xi) d\xi, \quad \bar{D}_y(x, y) = \int_{z_-(x,y)}^{z_+(x,y)} D_y(x, y, \xi) d\xi,$$

for $(x, y) \in \bar{\Omega}$, with $\bar{D}_x, \bar{D}_y \in C^1(\bar{\Omega})$ and bounded above zero on $\bar{\Omega}$. Finally $\hat{\mathbf{n}}(x, y) = (n_x(x, y), n_y(x, y))$ is the unit outward normal to the bounded 2-d domain Ω , and I_0 , α_i and $\hat{\alpha}_T$ are given by (2.26), (2.8) and (2.20), respectively.

It follows from (2.7) and (2.20) that

$$\iint_{\Omega} F(x, y) \, dx \, dy = 0, \quad (2.44)$$

and hence by classical theory for strongly elliptic boundary value problems (see for example (9)) that [BVP] has a unique solution. In particular, with $A : \bar{\Omega} \mapsto \mathbb{R}$ being the solution to [BVP], it is shown in (6, equation (3.18)) that

$$A(x, y) = \frac{-\alpha_i}{4\pi(\bar{D}_x^i \bar{D}_y^i)^{\frac{1}{2}}} \log \left[\frac{(x - x_i)^2}{\bar{D}_x^i} + \frac{(y - y_i)^2}{\bar{D}_y^i} \right] + A_0^i + O\left(\left([x - x_i]^2 + [y - y_i]^2\right)^{\frac{1}{2}}\right), \quad (2.45)$$

as $(x, y) \rightarrow (x_i, y_i)$, with $A_0^i \in \mathbb{R}$ being a globally determined constant and $\bar{D}_x^i = \bar{D}_x(x_i, y_i)$, $\bar{D}_y^i = \bar{D}_y(x_i, y_i)$, for $i = 1, \dots, N$.

In general, except for particularly simple boundaries $\partial\Omega$, permeabilities \bar{D}_x , \bar{D}_y , and line source/sink locations $(x_i, y_i) \in \partial\Omega$, $i = 1, \dots, N$, [BVP] will need to be solved numerically. However, [BVP] is a 2-d, regular, strongly elliptic problem, and numerical solution via finite element methods can be achieved rapidly and accurately. We defer detailed consideration of the numerical solution of [BVP] until §3.1.

It is shown in (6) that the outer region asymptotic expansions (2.37)–(2.40) become non-uniform when $\mathbf{r} \in \delta_i^c$ as $\epsilon \rightarrow 0$ ($i = 1, \dots, N$). To obtain a uniform asymptotic representation of the solution to [PSSP] when $\mathbf{r} \in \delta_i^c$ as $\epsilon \rightarrow 0$, we must therefore introduce an inner region at each line source/sink location $(x, y) = (x_i, y_i)$, $i = 1, \dots, N$. In the inner region we write $(x, y) = (x_i, y_i) + \epsilon(X, Y)$, with $(X, Y) \in \mathbb{R}^2$ such that $X, Y = O(1)$ as $\epsilon \rightarrow 0$, and we define (\tilde{R}_i, θ, z) to be local cylindrical polar coordinates based at $(X, Y, z) = (0, 0, 0)$, with $X = \tilde{R}_i \cos \theta$, $Y = \tilde{R}_i \sin \theta$ and $\tilde{R}_i = (X^2 + Y^2)^{1/2}$. For notational convenience we also define $z_{\pm}^i = z_{\pm}(x_i, y_i)$ and $\tilde{D}_{\alpha}(z) = D_{\alpha}(x_i, y_i, z)$, for $z \in [z_{-}^i, z_{+}^i]$ and $\alpha = x, y$ or z . Under the assumption

$$\tilde{D}_x(z) = \tilde{D}_y(z) =: \tilde{D}_h(z), \quad z \in [z_{-}^i, z_{+}^i],$$

so that permeability in the horizontal directions is equal at the well, but still dependent upon $z \in [z_{-}^i, z_{+}^i]$ (a consequence of which is that $\bar{D}_x^i = \bar{D}_y^i =: \bar{D}_h^i$), it follows that the asymptotic expansion for \hat{p} in the inner region is

$$\hat{p}(\tilde{R}_i, z; \epsilon) = \frac{-\alpha_i}{2\pi\bar{D}_h^i} \log \epsilon + F_i(\tilde{R}_i, z) + O(\epsilon) \quad (2.46)$$

as $\epsilon \rightarrow 0$, with $(\tilde{R}_i, z) \in (0, \infty) \times [z_{-}^i, z_{+}^i]$, and $F_i : (0, \infty) \times [z_{-}^i, z_{+}^i] \mapsto \mathbb{R}$ given by

$$F_i(\tilde{R}_i, z) = \left(A_0^i + \frac{\alpha_i}{4\pi\bar{D}_h^i} \log \bar{D}_h^i - \frac{\alpha_i}{2\pi\bar{D}_h^i} \log \tilde{R}_i \right) + \sum_{j=1}^{\infty} B_j K_0(\bar{\lambda}_j^{1/2} \tilde{R}_i) \psi_j(z), \quad (\tilde{R}_i, z) \in (0, \infty) \times [z_{-}^i, z_{+}^i]. \quad (2.47)$$

Here $K_{\nu}(\cdot)$ is the usual modified Bessel function of order ν (see (10, chapter 9)), while $\bar{\lambda}_r \in \mathbb{R}$ and $\psi_r : [z_{-}^i, z_{+}^i] \mapsto \mathbb{R}$ for $r = 0, 1, 2, \dots$ are the eigenvalues and corresponding

eigenfunctions of the regular Sturm-Liouville eigenvalue problem,

$$\left(\tilde{D}_z(z)\psi'(z)\right)' + \bar{\lambda}\tilde{D}_h(z)\psi(z) = 0, \quad z \in (z_-^i, z_+^i), \quad (2.48)$$

$$\psi'(z_-^i) = \psi'(z_+^i) = 0, \quad (2.49)$$

which we refer to as [SL]. The eigenvalues of [SL] have $0 = \bar{\lambda}_0 < \bar{\lambda}_1 < \bar{\lambda}_2 < \dots$, (see e.g. (11, chapters 7,8)) with $\bar{\lambda}_r \rightarrow \infty$ as $r \rightarrow \infty$, and the corresponding eigenfunctions are normalised so that

$$\langle \psi_j, \psi_k \rangle = \int_{z_-^i}^{z_+^i} \tilde{D}_h(s)\psi_j(s)\psi_k(s) ds = \delta_{jk}, \quad (2.50)$$

for $j, k = 0, 1, 2, \dots$. The constants B_r , $r = 1, 2, \dots$ are given by

$$B_r = \frac{1}{2\pi} \int_{z_-^i}^{z_+^i} s_i(\mu)\psi_r(\mu) d\mu, \quad r = 1, 2, \dots \quad (2.51)$$

The asymptotic expansions for the flow fields \hat{u} , \hat{v} , \hat{w} in the inner region are then given by

$$\hat{u}(X, Y, z; \epsilon) = \epsilon^{-1} \left(-\tilde{D}_x(z) \frac{X}{\tilde{R}_i} \left(\frac{-\alpha_i}{2\pi\tilde{D}_h^i \tilde{R}_i} - \sum_{j=1}^{\infty} B_j \bar{\lambda}_j^{1/2} K_1(\bar{\lambda}_j^{1/2} \tilde{R}_i) \psi_j(z) \right) + O(\epsilon) \right), \quad (2.52)$$

$$\hat{v}(X, Y, z; \epsilon) = \epsilon^{-1} \left(-\tilde{D}_y(z) \frac{Y}{\tilde{R}_i} \left(\frac{-\alpha_i}{2\pi\tilde{D}_h^i \tilde{R}_i} - \sum_{j=1}^{\infty} B_j \bar{\lambda}_j^{1/2} K_1(\bar{\lambda}_j^{1/2} \tilde{R}_i) \psi_j(z) \right) + O(\epsilon) \right), \quad (2.53)$$

$$\hat{w}(X, Y, z; \epsilon) = \epsilon^{-2} \left(-\tilde{D}_z(z) \sum_{j=1}^{\infty} B_j K_0(\bar{\lambda}_j^{1/2} \tilde{R}_i) \psi_j'(z) + O(\epsilon) \right). \quad (2.54)$$

The only remaining question is how to compute the eigenvalues and corresponding eigenfunctions of [SL]. This is straightforward and is addressed in §3.4. The asymptotic solution to [PSSP] as $\epsilon \rightarrow 0$ uniformly for $(x, y, z) \in \bar{M}'$ is now complete; details of how the solution is actually computed are presented in §§3.1–3.5.

2.2 Solution to [EVP]

We next turn our attention to the asymptotic solution to the eigenvalue problem [EVP] as $\epsilon \rightarrow 0$. It is shown in (6) that the eigenvalues λ_j and corresponding normalised eigenfunctions ϕ_j have the asymptotic expansions

$$\lambda_j(\epsilon) = \tilde{\lambda}_j [1 + O(\epsilon^2)], \quad \phi_j(x, y, z; \epsilon) = \tilde{A}_j(x, y) + O(\epsilon^2), \quad \text{as } \epsilon \rightarrow 0,$$

for $j = 0, 1, 2, \dots$, uniformly for $(x, y, z) \in \bar{M}'$, where $\tilde{A}_j : \bar{\Omega} \mapsto \mathbb{R}$ and $\tilde{\lambda}_j \in \mathbb{R}$ satisfy the regular self-adjoint eigenvalue problem,

$$\frac{\partial}{\partial x} \left(\bar{D}_x(x, y) \frac{\partial \tilde{A}}{\partial x}(x, y) \right) + \frac{\partial}{\partial y} \left(\bar{D}_y(x, y) \frac{\partial \tilde{A}}{\partial y}(x, y) \right) + \tilde{\lambda} \hat{\phi}(x, y) \tilde{A}(x, y) = 0, \quad (x, y) \in \Omega, \quad (2.55)$$

$$\bar{D}_x(x, y) \frac{\partial \tilde{A}}{\partial x}(x, y) n_x(x, y) + \bar{D}_y(x, y) \frac{\partial \tilde{A}}{\partial y}(x, y) n_y(x, y) = 0, \quad (x, y) \in \partial\Omega. \quad (2.56)$$

We refer to this eigenvalue problem as [EVP]’.

Classical theory (see for example (12)) determines that the set of eigenvalues of [EVP]’ is given by $\tilde{\lambda} = \tilde{\lambda}_r \in \mathbb{R}$, $r = 0, 1, 2, \dots$, with,

$$0 = \tilde{\lambda}_0 < \tilde{\lambda}_1 \leq \tilde{\lambda}_2 \leq \dots \quad (2.57)$$

and $\tilde{\lambda}_r = O(r^2)$ as $r \rightarrow \infty$. Corresponding to each eigenvalue $\tilde{\lambda}_r$ in the ordering (2.57) there is a unique normalised eigenfunction $\tilde{A}_r : \bar{\Omega} \mapsto \mathbb{R}$ such that

$$\int \int_{\Omega} \hat{\phi}(x, y) \tilde{A}_i(x, y) \tilde{A}_j(x, y) dx dy = \delta_{ij}, \quad (2.58)$$

for $i, j = 0, 1, 2, \dots$. Recalling (2.34) and (2.35), we then have

$$\tilde{p}(x, y, z, t) = \sum_{r=1}^{\infty} c_r e^{-\tilde{\lambda}_r t} \tilde{A}_r(x, y) + O(\epsilon^2 e^{-\tilde{\lambda}_1 t}, e^{-t/\epsilon^2}) \quad (2.59)$$

as $\epsilon \rightarrow 0$, uniformly for $(x, y, z, t) \in \bar{M}' \times [\delta, \infty)$, for any $\delta > 0$, where c_r , $r = 1, 2, \dots$, are given by

$$c_r = \int \int_{\Omega} \langle \tilde{p}_0 \rangle(\eta, \xi) \tilde{A}_r(\eta, \xi) d\eta d\xi, \quad (2.60)$$

with $\langle \tilde{p}_0 \rangle : \bar{\Omega} \mapsto \mathbb{R}$ given by

$$\langle \tilde{p}_0 \rangle(x, y) = \int_{z_-(x, y)}^{z_+(x, y)} \tilde{p}_0(x, y, s) \bar{\phi}(x, y, s) ds, \quad (x, y) \in \bar{\Omega}, \quad (2.61)$$

with $\tilde{p}_0 : \bar{M}' \mapsto \mathbb{R}$ given by (2.31). Thus $\tilde{p}(x, y, z, t) \sim (c_1 \tilde{A}_1(x, y) + O(\epsilon^2)) e^{-\tilde{\lambda}_1 t}$ as $t \rightarrow \infty$, uniformly for $(x, y, z) \in \bar{M}'$. Therefore, the transient part of the solution to [IBVP] decays exponentially with rate $\tilde{\lambda}_1$ as $t \rightarrow \infty$, with the dimensionless time scale for transient relaxation being $t_s \sim (\tilde{\lambda}_1)^{-1}$.

3. Computation of the pressure and velocity fields throughout the layer

We now describe the full algorithm for computing p , u , v , and w , via the asymptotic solution for $0 < \epsilon \ll 1$ to [IBVP], given by (2.1)–(2.4), (2.11)–(2.14). The most demanding computational steps are the numerical solution of [BVP] and [EVP]’; however, there are also a number of difficulties concerning the transfer of information from one part of the solution to another. The key steps of the algorithm are as follows:

- (i) Compute A solving [BVP], given by (2.41)–(2.43);
- (ii) Construct the outer region asymptotic expansions, given by (2.37)–(2.40);
- (iii) Compute the globally determined constant A_0^i from (2.45), for each $i = 1, \dots, N$;
- (iv) Compute the smallest strictly positive eigenvalues and their corresponding normalised eigenfunctions for the Sturm-Liouville eigenvalue problem [SL], given by (2.48)–(2.49);
- (v) Construct the inner region asymptotic expansions, given by (2.46), (2.47), (2.51)–(2.54);
- (vi) Compute the smallest strictly positive eigenvalues and their corresponding normalised eigenfunctions for the eigenvalue problem [EVP]’, given by (2.55), (2.56);

- (vii) Compute the transient pressure \tilde{p} , given by (2.59), via computation of the coefficients c_r , $r = 1, 2, \dots$, given by (2.60)–(2.61);
- (viii) Compute the approximations to the dimensionless fluid pressure and velocity fields, given by (2.16)–(2.19) and (2.6).

We outline the implementation (used to generate the numerical results of §4) for each of these steps in §§3.1–3.8.

3.1 Numerical solution of [BVP]

To solve [BVP], given by (2.41)–(2.43), we use a standard finite element method, with a piecewise linear approximation space on a quasi-uniform triangulation of the 2-d domain Ω . There is a very wide literature on the efficient implementation of finite element methods for the solution of elliptic problems such as this (see e.g. (13, 14)), but we provide some brief details here both for completeness and also to ease the explanation of the implementation details provided in §§3.2–3.8.

A weak formulation of (2.41)–(2.42) is: Find $A \in H^1(\Omega)$ such that

$$\int_{\Omega} \bar{D}_x \frac{\partial A}{\partial x} \frac{\partial v}{\partial x} + \bar{D}_y \frac{\partial A}{\partial y} \frac{\partial v}{\partial y} d\Omega = - \int_{\Omega} Fv d\Omega, \quad \text{for all } v \in H^1(\Omega). \quad (3.1)$$

We then seek an approximation to A in the finite dimensional space of piecewise linear functions on a triangulation of Ω , and we require (3.1) to hold for each v in the same finite dimensional space. More specifically, we triangulate the domain using N_t triangles Ω_i , $i = 1, \dots, N_t$, with corners $(\tilde{x}_i, \tilde{y}_i)$, $i = 1, \dots, N_e$ (for the numerical results in §4 we used the mesh generation routine described in (15)), so that $\Omega = \cup_{i=1}^{N_t} \bar{\Omega}_i \setminus \Gamma$, and we choose basis functions χ_i , $i = 1, \dots, N_e$, such that $\chi_i(\tilde{x}_j, \tilde{y}_j) = \delta_{ij}$, with $\chi_i(x, y)$ linear on each triangle. We then substitute

$$A(x, y) \approx \sum_{j=1}^{N_e} u_j \chi_j(x, y) \quad (3.2)$$

into (3.1) and require the resulting equation to hold for all $v \in S^h$, where S^h is the space of functions that are linear on each triangle Ω_i , $i = 1, \dots, N_t$, so that $S^h = \text{span}_{i=1, \dots, N_e} \{\chi_i\}$. This leads to the linear algebraic system

$$\begin{aligned} & \sum_{j=1}^{N_e} u_j \left[\int_{\Omega} \bar{D}_x \frac{\partial \chi_j}{\partial x} \frac{\partial \chi_m}{\partial x} + \bar{D}_y \frac{\partial \chi_j}{\partial y} \frac{\partial \chi_m}{\partial y} \right] d\Omega \\ & = \sum_{i=1}^N \alpha_i \chi_m(x_i, y_i) - \hat{\alpha}_T \iint_{\Omega} \hat{\phi}(x, y) \chi_m(x, y) dx dy, \quad m = 1, \dots, N_e. \end{aligned} \quad (3.3)$$

The system (3.3) cannot be solved directly, as we have not yet taken account of (2.43), and hence the coefficients u_i , $i = 1, \dots, N_e$ are not uniquely determined. However, the condition (2.43) corresponds to an additional constraint often applied to pure Neumann problems to deal with the nonuniqueness (see e.g. (16, chapter II §3)), and appending it to (3.3) to form a uniquely solvable system is straightforward. Substituting (3.2) into (2.43)

gives us

$$\sum_{j=1}^{N_e} u_j \iint_{\Omega} \hat{\phi}(x, y) \chi_j(x, y) \, dx \, dy = I_0.$$

Applying this immediately to (3.3) would lead to an overdetermined system, so to avoid this we add $\lambda \iint_{\Omega} \hat{\phi}(x, y) \chi_m(x, y) \, dx \, dy$ to the left hand side of (3.3) for each $m = 1, \dots, N_e$, to give a uniquely solvable $(N_e + 1) \times (N_e + 1)$ linear system for the unknowns $u_j, j = 1, \dots, N_e$ and λ , with $\lambda = 0$ returning (3.3) exactly. More specifically, we define the matrix $K = [K_{m,j}]$ $j, m = 1, \dots, N_e$ by

$$K_{m,j} = \int_{\Omega} \left[\bar{D}_x \frac{\partial \chi_j}{\partial x} \frac{\partial \chi_m}{\partial x} + \bar{D}_y \frac{\partial \chi_j}{\partial y} \frac{\partial \chi_m}{\partial y} \right] \, d\Omega, \quad j, m = 1, \dots, N_e, \quad (3.4)$$

the vector $\mathbf{f} = [f_1 \dots f_{N_e}]^T$ by

$$f_m = \sum_{i=1}^N \alpha_i \chi_m(x_i, y_i) - \hat{\alpha}_T \iint_{\Omega} \hat{\phi}(x, y) \chi_m(x, y) \, dx \, dy, \quad m = 1, \dots, N_e, \quad (3.5)$$

the vector $\mathbf{b} = [b_1 \dots b_{N_e}]^T$ by

$$b_m = \iint_{\Omega} \hat{\phi}(x, y) \chi_m(x, y) \, dx \, dy, \quad m = 1, \dots, N_e, \quad (3.6)$$

and we take $\mathbf{u} = [u_1 \dots u_{N_e}]^T$. The linear system that we solve for the unknown coefficients $u_j, j = 1, \dots, N_e$, of (3.2) is then

$$\begin{bmatrix} K & \mathbf{b} \\ \mathbf{b}^T & 0 \end{bmatrix} \begin{bmatrix} \mathbf{u} \\ \lambda \end{bmatrix} = \begin{bmatrix} \mathbf{f} \\ I_0 \end{bmatrix}. \quad (3.7)$$

To evaluate $\text{meas}(\bar{M}')$ (and hence $\hat{\alpha}_T$, recall (2.20)) and the integrals in (3.4), (3.5) and (3.6) it is often sufficient (see e.g. (13, p.182)) to use a simple rule such as the centroid rule on each triangle. If $\partial\Omega$ is curved and $\bar{\phi}$ is complicated then care is needed to ensure that the discrete version of (2.44) holds (see e.g. (17) for details). Noting that the matrix K in (3.7) is sparse and symmetric, we use the conjugate gradient scheme to solve (3.7) in §4, but we remark that a preconditioner could be used to speed up the solve further, see e.g. (18) and the references therein.

To compute the constant I_0 , given by (2.26), we decompose the integral over the 3-d domain M' into a sum of integrals over each triangle,

$$I_0 = \bar{p}_0 \sum_{j=1}^{N_t} \iint_{\Omega_j} \left[\int_{z_-(x,y)}^{z_+(x,y)} f(x, y, z) \bar{\phi}(x, y, z) \, dz \right] \, dx \, dy, \quad (3.8)$$

and then we compute the outer integrals in (3.8) using the centroid rule, and the inner integrals using Gaussian quadrature. This approach is appropriate under the assumption that the initial pressure variation $f(x, y, z)$ is smooth throughout the layer (recall (2.15)). If instead $f(x, y, z)$ is highly peaked near the wells, for example, as will be the case if the

initial pressure variation is given by the final solution from a previous run (if one wishes to consider the effect of varying production rates, for example, see §4), then the integration scheme outlined above may not be sufficiently accurate. In this case, a better approach would be to use a partition of unity to split the integral, so that the inner and outer regions can be considered separately, with the approach described above being appropriate for the outer region, and a more suitable graded mesh being used on each inner region in order to deal with the singular behaviour of the solution near the line sources/sinks. This is the approach used to compute the constants c_r , defined by (2.60), arising in the series representation for the transient pressure field \tilde{p} , given by (2.59), and full details are provided in §3.7 below.

3.2 Computation of outer region asymptotic expansions

Having solved [BVP], we are now in a position to construct the outer region asymptotic expansions, accurate to $O(\epsilon^2)$, given by (2.37)–(2.40), that is,

$$\begin{aligned} \hat{p}(x, y, z; \epsilon) &\approx A(x, y), \\ \hat{u}(x, y, z; \epsilon) &\approx -D_x(x, y, z) \frac{\partial A}{\partial x}(x, y), \\ \hat{v}(x, y, z; \epsilon) &\approx -D_y(x, y, z) \frac{\partial A}{\partial y}(x, y), \\ \hat{w}(x, y, z; \epsilon) &\approx \int_{z_-(x, y)}^z \left\{ \frac{\partial}{\partial x} \left(D_x(x, y, \xi) \frac{\partial A}{\partial x}(x, y) \right) + \frac{\partial}{\partial y} \left(D_y(x, y, \xi) \frac{\partial A}{\partial y}(x, y) \right) \right\} d\xi \\ &\quad - \hat{\alpha}_T \int_{z_-(x, y)}^z \bar{\phi}(x, y, \xi) d\xi. \end{aligned} \tag{3.9}$$

The approximation to the pseudo-steady state pressure field on the outer region, \hat{p} , follows immediately from our approximation to $A(x, y)$, but to find \hat{u} , \hat{v} and \hat{w} we need to do a bit more work.

To approximate \hat{u} , rather than differentiating the function $A(x, y)$ explicitly (which would lead to a piecewise constant approximation, discontinuous across element boundaries), we instead write $\hat{u}(x, y, z; \epsilon) \approx \sum_{i=1}^{N_e} \hat{u}_i(z; \epsilon) \chi_i(x, y)$, and determine the functions $\hat{u}_i(z; \epsilon)$ (which will provide an approximation to $\hat{u}(\tilde{x}_i, \tilde{y}_i, z; \epsilon)$) by solving a weak form of

$$\sum_{i=1}^{N_e} \hat{u}_i(z; \epsilon) \chi_i(x, y) = -D_x(x, y, z) \frac{\partial A}{\partial x}(x, y),$$

specifically (recalling (3.2))

$$\sum_{i=1}^{N_e} \hat{u}_i(z; \epsilon) \iint_{\Omega} \chi_i(x, y) \chi_m(x, y) dx dy = -\sum_{j=1}^{N_e} u_j \iint_{\Omega} D_x(x, y, z) \frac{\partial \chi_j(x, y)}{\partial x} \chi_m(x, y) dx dy, \tag{3.10}$$

for $m = 1, \dots, N_e$. To determine $\hat{u}_i(z; \epsilon)$, $i = 1, \dots, N_e$, from (3.10), we use a form of mass lumping. We define $\Pi^h : C(\bar{\Omega}) \mapsto S^h$ to be the linear interpolation operator from the space of continuous functions on $\bar{\Omega}$ to the space of functions that are linear on each triangle

Ω_i , so that for $v \in C(\bar{\Omega})$, $\Pi^h v(\tilde{x}_j, \tilde{y}_j) = v(\tilde{x}_j, \tilde{y}_j)$, $j = 1, \dots, N_e$, and then $\Pi^h v(x, y) = \sum_{i=1}^{N_e} \chi_i(x, y) v(\tilde{x}_i, \tilde{y}_i)$. Thus

$$\Pi^h \{\chi_j(x, y) \chi_m(x, y)\} = \sum_{i=1}^{N_e} \chi_i(x, y) \chi_j(\tilde{x}_i, \tilde{y}_i) \chi_m(\tilde{x}_i, \tilde{y}_i) = \delta_{jm} \chi_j(x, y),$$

and hence if we approximate the integrals on the left hand side of (3.10) using

$$\iint_{\Omega} \chi_i(x, y) \chi_m(x, y) dx dy \approx \iint_{\Omega} \Pi^h \{\chi_i(x, y) \chi_m(x, y)\} dx dy,$$

we end up with a diagonal system, allowing us to read off the functions $\hat{u}_m(z; \epsilon)$, $m = 1, \dots, N_e$, line by line. In the numerical results of §4 we evaluate the integrals on the right hand side of (3.10) using the centroid rule on each triangle.

The procedure for approximating \hat{v} is identical. To approximate \hat{w} we define

$$\begin{aligned} \check{D}_x(x, y, z) &= \int_{z_-(x, y)}^z D_x(x, y, \xi) d\xi, & \check{D}_y(x, y, z) &= \int_{z_-(x, y)}^z D_y(x, y, \xi) d\xi, \\ \check{\phi}(x, y, z) &= \int_{z_-(x, y)}^z \bar{\phi}(x, y, \xi) d\xi, \end{aligned}$$

so that the formula for \hat{w} becomes

$$\hat{w}(x, y, z; \epsilon) \approx \frac{\partial}{\partial x} \left(\check{D}_x(x, y, z) \frac{\partial A}{\partial x}(x, y) \right) + \frac{\partial}{\partial y} \left(\check{D}_y(x, y, z) \frac{\partial A}{\partial y}(x, y) \right) - \hat{\alpha}_T \check{\phi}(x, y, z).$$

Writing $\hat{w}(x, y, z; \epsilon) \approx \sum_{i=1}^{N_e} \hat{w}_i(z; \epsilon) \chi_i(x, y)$ and following similar steps to those described for the computation of \hat{u} above, we obtain

$$\begin{aligned} & \sum_{i=1}^{N_e} \hat{w}_i(z; \epsilon) \iint_{\Omega} \chi_i(x, y) \chi_m(x, y) dx dy \\ &= - \sum_{j=1}^{N_e} u_j \left(\int_{\Omega} \check{D}_x \frac{\partial \chi_j}{\partial x} \frac{\partial \chi_m}{\partial x} + \check{D}_y \frac{\partial \chi_j}{\partial y} \frac{\partial \chi_m}{\partial y} \right) d\Omega - \hat{\alpha}_T \iint_{\Omega} \check{\phi}(x, y, z) \chi_m(x, y) dx dy, \end{aligned} \tag{3.11}$$

for $m = 1, \dots, N_e$, where we have used the boundary condition

$$D_x(x, y, z) \frac{\partial A}{\partial x}(x, y) n_x(x, y) + D_y(x, y, z) \frac{\partial A}{\partial y}(x, y) n_y(x, y) = 0, \quad \mathbf{r} \in \partial M'_H,$$

which follows from (2.23) (see (6, §3) for details). We determine the functions $\hat{w}_i(z; \epsilon)$ from (3.11) in an identical fashion to the computation of $\hat{u}_i(z; \epsilon)$ from (3.10) above.

3.3 Computation of A_0^i

Having computed the solution to [BVP], and hence the leading order terms in the outer region asymptotic expansions for the pressure and flow fields, it now remains to compute the

solutions in the inner regions, around each line source/sink. For each $i = 1, \dots, N$, where N is the number of line sources and sinks, we first need to compute the globally determined constant A_0^i from (2.45). Writing $R_i = ((x - x_i)^2 + (y - y_i)^2)^{1/2}$, for each $i = 1, \dots, N$, (2.45) can be written as

$$A(x, y) + \frac{\alpha_i}{4\pi(\bar{D}_x^i \bar{D}_y^i)^{\frac{1}{2}}} \log \left[\frac{(x - x_i)^2}{\bar{D}_x^i} + \frac{(y - y_i)^2}{\bar{D}_y^i} \right] = A_0^i + O(R_i), \quad \text{as } R_i \rightarrow 0. \quad (3.12)$$

To determine an approximation to A_0^i , we evaluate the left hand side of (3.12) for certain values of x and y corresponding to a decreasing sequence of values of R_i , and then we compute the best fitting (in a least squares sense) linear approximation to the left hand side (as a function of R_i). Our approximation to A_0^i is then given by the constant term in this approximation. Equation (3.12) suggests that, in a neighbourhood of the line source/sink at (x_i, y_i) , the left hand side depends only on R_i , the distance from (x_i, y_i) , but in practice the value will depend to some extent on the direction in which we take our coordinates x and y . Our algorithm is thus as follows. We begin by determining a range of values of R_i over which (3.12) is to be evaluated. Defining \hat{h} to be the maximum side length of the triangles in our mesh, we evaluate (3.12) for $R_i = j\hat{h}$, $j = 1, \dots, M$, with M an experimentally chosen constant ($M = 5$ seems to strike a good balance between speed and accuracy, for the examples tested), in each of the four coordinate directions (moving in positive and negative directions parallel to the x and y axes). More specifically, we compute the left hand side of (3.12) in each of the four cases:

$$(x, y) = (x_i \pm j\hat{h}, y_i), \quad (x, y) = (x_i, y_i \pm j\hat{h}), \quad j = 1, \dots, M,$$

and then we determine the best fitting linear approximation to the left hand side of (3.12) as a function of R_i , in each of these four cases. This gives four approximations to A_0^i . Provided they are all reasonably close to one another (using a prescribed tolerance value), our approximation to A_0^i is taken to be the mean of the four values. If the four values differ significantly, then this would suggest that (3.12) is not sufficiently well resolved in terms of the numerical approximation to A , suggesting that A should be recomputed on a finer grid.

3.4 Numerical solution of [SL]

Next, for each $i = 1, \dots, N$, we need to find the smallest strictly positive eigenvalues and their corresponding eigenfunctions for the Sturm-Liouville eigenvalue problem [SL], given by (2.48)–(2.49). To solve this problem we employ a standard finite element scheme, with a piecewise linear approximation space on a uniform decomposition of the interval $[z_-^i, z_+^i]$. First we multiply (2.48) by a test function $\tilde{\chi} \in H^1(z_-^i, z_+^i)$ and integrate by parts, noting the boundary conditions (2.49), to get

$$\int_{z_-^i}^{z_+^i} \tilde{D}_z(z) \psi'(z) \tilde{\chi}(z) dz = \bar{\lambda} \int_{z_-^i}^{z_+^i} \tilde{D}_h(z) \psi(z) \tilde{\chi}(z) dz. \quad (3.13)$$

For $M_{SL} > 1$ we then define a uniform mesh on $[z_-^i, z_+^i]$ by $\tilde{z}_j = z_-^i + j(z_+^i - z_-^i)/M_{SL}$, $j = 0, \dots, M_{SL}$, and we define $\tilde{\chi}_j$, $j = 0, \dots, M_{SL}$, to be linear on each interval $(\tilde{z}_{j-1}, \tilde{z}_j)$,

$j = 1, \dots, M_{SL}$, with $\tilde{\chi}_j(\tilde{z}_m) = \delta_{jm}$. We then replace ψ in (3.13) with ψ^M defined by

$$\psi^M(z) = \sum_{j=0}^{M_{SL}} \tilde{\chi}_j(z) \psi^M(\tilde{z}_j), \quad (3.14)$$

and require this equation to hold for each $\tilde{\chi} = \tilde{\chi}_m$, $m = 0, \dots, M_{SL}$, leading to the linear system

$$\tilde{K} \mathbf{v} = \bar{\lambda} \tilde{M} \mathbf{v}, \quad (3.15)$$

where $\mathbf{v} = [\psi^M(\tilde{z}_0) \dots \psi^M(\tilde{z}_{M_{SL}})]^T$, $\tilde{K} = [\tilde{K}_{m,j}]$ and $\tilde{M} = [\tilde{M}_{m,j}]$, $j, m = 0, \dots, M_{SL}$, with

$$\tilde{K}_{m,j} = \int_{z_-^i}^{z_+^i} \tilde{D}_z(z) \tilde{\chi}_j'(z) \tilde{\chi}_m'(z) dz, \quad j, m = 0, \dots, M_{SL}, \quad (3.16)$$

$$\tilde{M}_{m,j} = \int_{z_-^i}^{z_+^i} \tilde{D}_h(z) \tilde{\chi}_j(z) \tilde{\chi}_m(z) dz, \quad j, m = 0, \dots, M_{SL}. \quad (3.17)$$

The matrix \tilde{K} is tridiagonal, and for the results of §4 we evaluate the integrals (3.16) using the trapezoidal rule with \tilde{z}_j , $j = 0, \dots, M_{SL}$ as the nodes. To evaluate \tilde{M} we use an analogous procedure to that described in §3.2 of replacing the integrand in (3.17) by its piecewise linear interpolant, which leads to a diagonal matrix. The first few eigenvalues of [SL] are then approximated by the first few eigenvalues of $\tilde{M}^{-1} \tilde{K}$, and the eigenfunctions of [SL] are approximated using (3.14) with \mathbf{v} the corresponding eigenvectors of $\tilde{M}^{-1} \tilde{K}$. It then just remains to normalise the eigenfunctions, using (2.50). Given an eigenfunction ψ^M , the normalised eigenfunction is given by

$$\tilde{\psi}^M = \frac{\psi^M}{\sqrt{\int_{z_-^i}^{z_+^i} \tilde{D}_h(s) [\psi^M(s)]^2 ds}}. \quad (3.18)$$

Since our solution of (3.15) gives an approximation to $\mathbf{v} = [\psi^M(\tilde{z}_0) \dots \psi^M(\tilde{z}_{M_{SL}})]^T$, it is appropriate to approximate the integral in the denominator on the right hand side of (3.18) using the trapezoidal rule with \tilde{z}_j , $j = 0, \dots, M_{SL}$ as the nodes.

3.5 Computation of \hat{p} in inner region

We can now compute an approximation to \hat{p} in the inner region, using (2.46), that is

$$\hat{p}(\tilde{R}_i, z; \epsilon) \approx \frac{-\alpha_i}{2\pi \tilde{D}_h^i} \log \epsilon + F_i(\tilde{R}_i, z), \quad (3.19)$$

where $F_i(\tilde{R}_i, z)$ is given by (2.47) with the constants B_j , $j = 1, 2, \dots$, given by (2.51), approximated again using the trapezoidal rule with \tilde{z}_m , $m = 0, \dots, M_{SL}$ as the nodes, and our approximations to A_0^i and $\bar{\lambda}_j$, ψ_j , $j = 1, 2, \dots$, are computed as in §3.3 and §3.4. The choice of how many terms one should take in the summation on the right hand side of (2.47) depends to a large extent on how quickly $\bar{\lambda}_j$ increases with respect to j . However we note that the convergence rate is exponential in $\bar{\lambda}_j$ as $j \rightarrow \infty$. We can then compute the leading order terms in the asymptotic expansions for the flow field \hat{u} , \hat{v} , \hat{w} , in the inner region, using the formulae (2.52)–(2.54), with B_j , $\bar{\lambda}_j$, ψ_j , $j = 1, 2, \dots$, as described above, and our approximation to $\psi_j'(z)$ computed directly from (3.14).

3.6 Solution of [EVP]'

Having computed the inner region solutions, the next step is to solve [EVP]', to find the eigenvalues $\tilde{\lambda}$ and the corresponding eigenfunctions \tilde{A} required for the evaluation of the transient pressure field. We remark that the solution of [EVP]' does not depend on the location or number of sources/sinks, but only on the geometry, permeability and porosity of the layer. Hence, if one wishes to consider the solution of [IBVP] for various configurations of sources/sinks, but for a fixed geometry then there is no need to repeat any of the computations associated with [EVP]'.

As for [BVP] (recall §3.1) we also solve [EVP]' using a standard finite element method, with a piecewise linear approximation space on the same triangulation of the domain Ω . Again we begin by multiplying (2.55) by a test function $v \in H^1(\Omega)$, and integrating over Ω , to obtain the weak formulation

$$\int_{\Omega} \bar{D}_x \frac{\partial \tilde{A}}{\partial x} \frac{\partial v}{\partial x} + \bar{D}_y \frac{\partial \tilde{A}}{\partial y} \frac{\partial v}{\partial y} d\Omega = \tilde{\lambda} \int_{\Omega} \hat{\phi} \tilde{A} v d\Omega, \quad \text{for all } v \in H^1(\Omega), \quad (3.20)$$

i.e. we have the same left hand side as (3.1), but a different right hand side. Setting

$$\tilde{A}(x, y) = \sum_{j=1}^{N_e} \tilde{a}_j \chi_j(x, y), \quad (3.21)$$

and requiring (3.20) to hold for $v = \chi_m$, $m = 1, \dots, N_e$, as in §3.1, we arrive at the linear system

$$K \tilde{\mathbf{a}} = \tilde{\lambda} M \tilde{\mathbf{a}},$$

where $\tilde{\mathbf{a}} = [\tilde{a}_1 \dots \tilde{a}_{N_e}]^T$, K is given by (3.4), and $M = [M_{m,j}]$, $j, m = 1, \dots, N_e$, with

$$M_{m,j} = \iint_{\Omega} \hat{\phi}(x, y) \chi_j(x, y) \chi_m(x, y) dx dy, \quad j, m = 1, \dots, N_e.$$

To evaluate the mass matrix M , we use a similar form of mass lumping to that described in §3.2. With $\Pi^h : C(\bar{\Omega}) \mapsto S^h$ again denoting the linear interpolation operator from the space of continuous functions on $\bar{\Omega}$ to the space of functions that are linear on each triangle Ω_i , we approximate the mass matrix M using the formula

$$\begin{aligned} \iint_{\Omega} \hat{\phi}(x, y) \chi_j(x, y) \chi_m(x, y) dx dy &\approx \iint_{\Omega} \Pi^h \{ \hat{\phi}(x, y) \chi_j(x, y) \chi_m(x, y) \} dx dy, \\ &= \begin{cases} \hat{\phi}(\tilde{x}_j, \tilde{y}_j) \iint_{\Omega} \chi_j(x, y) dx dy, & \text{if } j = m, \\ 0, & \text{if } j \neq m. \end{cases} \end{aligned} \quad (3.22)$$

The first few eigenvalues of [EVP]' are then approximated by the first few eigenvalues of $M^{-1}K$, with the eigenvectors $\tilde{\mathbf{a}}$ providing the coefficients for the eigenfunctions \tilde{A} of [EVP]'.

It remains to normalise these eigenfunctions, via (2.58). Given an eigenfunction $\tilde{A}(x, y)$, the normalised eigenfunction is given by

$$\bar{A}(x, y) = \frac{\tilde{A}(x, y)}{\sqrt{\iint_{\Omega} \hat{\phi}(x, y) [\tilde{A}(x, y)]^2 dx dy}}. \quad (3.23)$$

To approximate the integral in the denominator on the right hand side of (3.23) we use the same procedure applied in (3.22), i.e. we replace the integrand by its piecewise linear interpolant on the triangulation of $\bar{\Omega}$. This allows us to reuse some of the computations required in the setting up of the mass matrix for [EVP]'. Specifically, recalling (3.21), we have

$$\begin{aligned} \iint_{\Omega} \hat{\phi}(x, y) [\tilde{A}(x, y)]^2 dx dy &\approx \iint_{\Omega} \Pi^h \left\{ \hat{\phi}(x, y) \left(\sum_{j=1}^{N_e} \tilde{a}_j \chi_j(x, y) \right)^2 \right\} dx dy, \\ &= \sum_{j=1}^{N_e} \tilde{a}_j^2 \left(\hat{\phi}(\tilde{x}_j, \tilde{y}_j) \iint_{\Omega} \chi_j(x, y) dx dy \right). \end{aligned}$$

Comparing with (3.22) it is clear that the integral in the denominator on the right hand side of (3.23) can be computed with only a very small number of additional calculations.

3.7 Computation of transient pressure \tilde{p}

Having solved [EVP]' and normalised the eigenfunctions, the remaining step in the computation of the transient pressure field \tilde{p} is the computation of the coefficients c_r , $r = 1, 2, \dots$, given by (2.60)–(2.61). Recalling (2.31) we write c_r as a sum of two integrals, $c_r = I_1 + I_2$, where

$$\begin{aligned} I_1 &= \iint_{\Omega} \left[\int_{z_-(x,y)}^{z_+(x,y)} \bar{p}_0 f(x, y, z) \bar{\phi}(x, y, z) dz \right] \tilde{A}_r(x, y) dx dy, \\ I_2 &= \iint_{\Omega} \left[\int_{z_-(x,y)}^{z_+(x,y)} \hat{p}(x, y, z) \bar{\phi}(x, y, z) dz \right] \tilde{A}_r(x, y) dx dy. \end{aligned}$$

For the case that the initial pressure variation $f(x, y, z)$ is smooth throughout the layer (recall (2.15)), computation of I_1 follows analogously to the computation of I_0 , described in §3.1 (see (3.8)). The only difference here is the presence of the term $\tilde{A}_r(x, y)$ in the integrand, but this poses no additional difficulties to the application of the centroid rule on each triangle. Moreover, there is considerable scope here to store and reuse some of the computations required in the evaluation of I_0 . If $f(x, y, z)$ is highly peaked near the line sources/sinks, the approach described below for the evaluation of I_2 can be equally well applied to the evaluation of I_1 .

To evaluate I_2 we need to use a different approach, due to the singular behaviour of $\hat{p}(x, y, z)$ at the line sources/sinks. We begin by defining, for $x \in [0, \infty)$ and $0 < x_0 < x_1$, the infinitely smooth ‘‘neutralising’’ function

$$S(x, x_0, x_1) = \begin{cases} 1 & \text{for } x \leq x_0, \\ \exp\left(\frac{2 \exp(-1/u)}{u-1}\right) & \text{for } x_0 < x < x_1, \quad u = \frac{x-x_0}{x_1-x_0}, \\ 0 & \text{for } x \geq x_1. \end{cases}$$

We will use this function to split the domain of integration for I_2 , so that the inner and outer regions can be considered separately, with the approach described above for the evaluation

of I_1 being appropriate for the outer region, and a more suitable graded mesh being used to evaluate the integrals on the inner region in order to deal with the singular behaviour there. Specifically, we choose constants $0 < a < b$, where $a, b = O(\epsilon)$, and we write $I_2 = \sum_{j=1}^{N+1} I_2^j$, where for $j = 1, \dots, N$,

$$I_2^j = \iint_{\Omega} \left[\int_{z_-(x,y)}^{z_+(x,y)} \hat{p}(x, y, z) \bar{\phi}(x, y, z) dz \right] S(R_j(x, y), a, b) \tilde{A}_r(x, y) dx dy$$

and

$$I_2^{N+1} = \iint_{\Omega} \left[\int_{z_-(x,y)}^{z_+(x,y)} \hat{p}(x, y, z) \bar{\phi}(x, y, z) dz \right] \left(1 - \sum_{j=1}^N S(R_j(x, y), a, b) \right) \tilde{A}_r(x, y) dx dy,$$

where $R_j(x, y) = \sqrt{(x - x_j)^2 + (y - y_j)^2}$ for each $j = 1, \dots, N$. The point of this splitting is that $S(R_j(x, y), a, b) = 0$ for $R_j(x, y) \geq b$, and hence the integrand for each I_2^j , for $j = 1, \dots, N$, is only supported for (x, y) inside a circle of radius b around the j^{th} line source/sink. These are the ‘‘inner’’ integrals. The integrand for I_2^{N+1} is equal to zero when (x, y) is a distance less than a from a line source/sink. This is the ‘‘outer’’ integral, and as it is only supported away from the line source/sinks it has no singularities and hence can be evaluated using a similar procedure to that for the evaluation of I_1 described above.

To evaluate I_2^j , for $j = 1, \dots, N$, we use the leading terms in the asymptotic expansion for \hat{p} in the inner region, given by (3.19), to get

$$\begin{aligned} I_2^j \approx & \tilde{A}_r(x_j, y_j) \iint_{\Omega} S(R_j(x, y), a, b) \left[\left(A_0^j + \frac{\alpha_j}{4\pi \bar{D}_h} \log \left(\frac{\bar{D}_h^j}{R_j(x, y)^2} \right) \right) \hat{\phi}(x_j, y_j) \right. \\ & \left. + \sum_{m=1}^{\infty} B_m K_0 \left(\bar{\lambda}_m^{1/2} \frac{R_j(x, y)}{\epsilon} \right) \int_{z_-(x_j, y_j)}^{z_+(x_j, y_j)} \psi_m(z) \bar{\phi}(x_j, y_j, z) dz \right] dx dy. \end{aligned}$$

Noting the radial symmetry of the integrand, we then have

$$\begin{aligned} I_2^j \approx & 2\pi \tilde{A}_r(x_j, y_j) \left[\hat{\phi}(x_j, y_j) \left(A_0^j + \frac{\alpha_j}{2\pi \bar{D}_h} \left(\frac{1}{2} \log(\bar{D}_h^j) \int_0^b S(R, a, b) R dR \right. \right. \right. \\ & \left. \left. - \int_0^b \log(R) S(R, a, b) R dR \right) \right) \\ & \left. + \sum_{m=1}^{\infty} B_m \int_0^b K_0 \left(\bar{\lambda}_m^{1/2} \frac{R}{\epsilon} \right) S(R, a, b) R dR \int_{z_-(x_j, y_j)}^{z_+(x_j, y_j)} \psi_m(z) \bar{\phi}(x_j, y_j, z) dz \right]. \end{aligned} \quad (3.24)$$

We now consider the evaluation of each of the four remaining integrals on the right hand side of (3.24) in turn. For the first two integrals, we integrate exactly over $(0, a)$, and use the trapezoidal rule on (a, b) , noting that $b - a = O(\epsilon)$, to get

$$\int_0^b S(R, a, b) R dR = \int_0^a R dR + \int_a^b S(R, a, b) R dR \approx \frac{ab}{2},$$

and

$$\int_0^b \log(R) S(R, a, b) R \, dR = \int_0^a R \log(R) \, dR + \int_a^b \log(R) S(R, a, b) R \, dR \approx \frac{a}{2} \left(b \log a - \frac{a}{2} \right).$$

To evaluate $\int_{z_-(x_j, y_j)}^{z_+(x_j, y_j)} \psi_m(z) \bar{\phi}(x_j, y_j, z) \, dz$ we use the composite trapezoidal rule exactly as for the evaluation of the constants B_r (see §3.5), recalling that $\psi_m(z)$ is already stored on an evenly spaced grid. Finally it just remains to compute the integrals

$$\int_0^b K_0 \left(\bar{\lambda}_m^{1/2} \frac{R}{\epsilon} \right) S(R, a, b) R \, dR. \quad (3.25)$$

Noting the limiting form of $K_0(\cdot)$ for a small argument (**10**, equation (9.6.8)), we have that $K_0(R) \sim -\log R$ as $R \rightarrow 0$, and thus the integrand in (3.25) has a weak singularity. Many approaches are available for evaluating singular integrals of this form (see e.g. (**19**) and the references therein). Here we use a composite quadrature rule on a graded mesh. Specifically, we divide the interval $(0, b)$ into $L + 1$ intervals, the first being $(0, b(0.15)^L)$, and the others being $(b(0.15)^{L+1-j}, b(0.15)^{L-j})$, $j = 1, \dots, L$, and then we evaluate the integral on each of these intervals using standard Gaussian quadrature, with L quadrature points on each interval. The convergence rate of this approach matches that of the underlying Gaussian quadrature scheme (**20**).

Having computed the eigenvalues $\tilde{\lambda}_r$ and corresponding normalised eigenfunctions \tilde{A}_r for [EVP]', for $r = 1, \dots, M_e$, and also the coefficients c_r , again for $r = 1, \dots, M_e$, we can then compute an approximation to the transient pressure field \tilde{p} via (2.59), specifically

$$\tilde{p}(x, y, z, t) \approx \sum_{r=1}^{M_e} c_r e^{-\tilde{\lambda}_r t} \tilde{A}_r(x, y).$$

3.8 Solution to [IBVP]

Having solved the pseudo-steady state problem [PSSP] and the evolutionary problem as described above, it just remains to put these solutions together via (2.16)–(2.19) to obtain our approximations to \bar{p} , u , v , and w solving [IBVP]. The formulae for $\bar{p}(\mathbf{r}, t)$ and $w(\mathbf{r}, t)$ follow immediately from our results above, noting from (2.59) that $\frac{\partial \tilde{p}}{\partial z}(\mathbf{r}, t) = 0$ to leading order. To compute our approximations to $u(\mathbf{r}, t)$ and $v(\mathbf{r}, t)$, we need to determine

$$\frac{\partial \tilde{p}}{\partial x}(\mathbf{r}, t) \approx \sum_{r=1}^{M_e} c_r e^{-\tilde{\lambda}_r t} \frac{\partial \tilde{A}_r}{\partial x}(x, y) \quad \text{and} \quad \frac{\partial \tilde{p}}{\partial y}(\mathbf{r}, t) \approx \sum_{r=1}^{M_e} c_r e^{-\tilde{\lambda}_r t} \frac{\partial \tilde{A}_r}{\partial y}(x, y).$$

To do this, we could just compute $\partial \tilde{A}_r(x, y)/\partial x$ and $\partial \tilde{A}_r(x, y)/\partial y$ directly from the formula (3.21), for each $r = 1, \dots, M_e$, but this would lead to a piecewise constant approximation to $\partial \tilde{p}/\partial x$ and $\partial \tilde{p}/\partial y$, discontinuous across element boundaries. Instead, recalling (2.33) we write

$$\tilde{u}_r = -D_x(x, y, z) \frac{\partial \tilde{A}_r}{\partial x}(x, y), \quad \text{and} \quad \tilde{v}_r = -D_y(x, y, z) \frac{\partial \tilde{A}_r}{\partial y}(x, y),$$

and then we compute approximations to \tilde{u}_r and \tilde{v}_r using a procedure identical to that used for the determination of $\tilde{u}(\mathbf{r})$ and $\tilde{v}(\mathbf{r})$, as described in §3.2. We do not repeat the details here. The final formula for $p(x, y, z, t)$, the dimensionless pressure field, is given by (2.6).

4. Numerical examples

For all of the examples in this section \overline{M}' is given by (2.5), with Ω the ellipse $\Omega = \{(x, y) : x^2 + 4y^2 < 1\}$, and the variable upper and lower boundaries given by

$$z_+(x, y) = \frac{1}{2}(x^2 + 4y^2) + \frac{1}{2}, \quad \text{and} \quad z_-(x, y) = -\frac{1}{2}(x^2 + 4y^2) - \frac{1}{2},$$

for $x, y \in \overline{\Omega}$. The permeability of the layer is nonuniform, with

$$D_x(x, y, z) = D_y(x, y, z) = \frac{1}{2}(x^2 + 4y^2 + 1)(2 + z), \quad D_z(x, y, z) = \frac{1}{2}(2 + z),$$

for $(x, y, z) \in \overline{M}'$. Finally, we take the dimensionless parameter $\epsilon = 0.01$. Recalling (2.10), this corresponds to e.g. horizontal and vertical length scales of $l = 100$ and $h = 1$ respectively, and permeability scales in the horizontal and vertical directions $D_0^H = D_0^L = 1$ respectively, all associated with the dimensional reservoir.

EXAMPLE 4.1 (Single line sink, constant porosity and initial pressure). For our first example, we take the porosity and initial pressure variation to be uniform throughout the layer, with $\bar{\phi}(x, y, z) = 1$ and $f(x, y, z) = 1$, for $(x, y, z) \in \overline{M}'$, and we consider the case of a single line sink at $(x_1, y_1) = (0, 0) \in \Omega$ with volumetric strength

$$s_1(z) = -6(z_+ - z)(z - z_-), \tag{4.1}$$

and hence $\alpha_1 = -1$, $\bar{p}_0 = 1$.

The computation of the remaining important quantities ($\text{meas}(\overline{M}')$ (and hence I_0 , in this case), A_0^1 , B_j , $\bar{\lambda}_j$, c_j and $\tilde{\lambda}_j$, for $j = 1, 2, \dots$) then depends on the values of the various discretisation parameters discussed in §3. In particular: our approximations to $\bar{\lambda}_j$ and B_j , for $j = 1, 2, \dots$, depend on the number of degrees of freedom M_{SL} used in the solution of [SL]; our approximations to $\text{meas}(\overline{M}')$, A_0^1 and $\tilde{\lambda}_j$, for $j = 1, 2, \dots$, depend on the maximum side length, \hat{h} , of the triangles used to discretise Ω ; our approximations to c_j , for $j = 1, 2, \dots$, depend on both \hat{h} and on the parameter L used to define the graded mesh for the approximation of the singular integrals arising in the formula for c_j , as described in §3.7. We thus begin by investigating what might be good choices for the values of these parameters.

First, we choose $\hat{h} = 0.01$, so that our mesh has $N_e = 18134$ nodes and $N_t = 35779$ triangles, and we investigate how the values of the first five constants c_j , $j = 1, \dots, 5$, depend on the choice of the parameter L , as described above. The values of c_j for $j = 1, \dots, 5$, and for $L = 1, 2, 3, 4$ are shown in Table 1. These results suggest that a small value of L such as $L = 3$ should be sufficient to evaluate the integrals (3.25) to a reasonable level of accuracy. Note that the total number of quadrature points used in this scheme for a fixed value of L is $L(L + 1)$, and that the integrand is only supported on an interval of length $O(\epsilon)$.

In Table 2 we consider the approximations to $\bar{\lambda}_j$ and B_j , for $j = 1, 2, \dots$, for various values of the parameter M_{SL} , the number of degrees of freedom required for the solution of [SL]. The results in Table 2 suggest that choosing $M_{SL} \geq 80$ should be sufficient to determine the eigenvalues, eigenfunctions, and coefficients B_j , $j = 1, 2, \dots$, to a reasonable level of accuracy.

| | $L = 1$ | $L = 2$ | $L = 3$ | $L = 4$ |
|-------|--------------------------|--------------------------|--------------------------|--------------------------|
| c_1 | 1.7764×10^{-7} | 1.7764×10^{-7} | 1.7764×10^{-7} | 1.7764×10^{-7} |
| c_2 | -1.8218×10^{-6} | -2.4005×10^{-6} | -2.1100×10^{-6} | -2.1141×10^{-6} |
| c_3 | -5.5934×10^{-2} | -5.5863×10^{-2} | -5.5845×10^{-2} | -5.5855×10^{-2} |
| c_4 | 1.1862×10^{-7} | 1.1863×10^{-7} | 1.1863×10^{-7} | 1.1863×10^{-7} |
| c_5 | -7.2958×10^{-8} | -7.2959×10^{-8} | -7.2959×10^{-8} | -7.2959×10^{-8} |

Table 1 Dependence of c_j , $j = 1, \dots, 5$, on the value of the mesh grading parameter L , for fixed \hat{h} .

| | $M_{SL} = 10$ | $M_{SL} = 20$ | $M_{SL} = 40$ | $M_{SL} = 80$ | $M_{SL} = 160$ |
|-------------------|-------------------------|-------------------------|-------------------------|-------------------------|-------------------------|
| λ_1 | 9.9660×10^0 | 1.0040×10^1 | 1.0057×10^1 | 1.0061×10^1 | 1.0062×10^1 |
| $\bar{\lambda}_2$ | 3.8114×10^1 | 3.9321×10^1 | 3.9592×10^1 | 3.9656×10^1 | 3.9671×10^1 |
| $\bar{\lambda}_3$ | 8.1232×10^1 | 8.7227×10^1 | 8.8596×10^1 | 8.8921×10^1 | 8.9000×10^1 |
| $\bar{\lambda}_4$ | 1.3412×10^2 | 1.5245×10^2 | 1.5676×10^2 | 1.5778×10^2 | 1.5803×10^2 |
| $\bar{\lambda}_5$ | 1.9041×10^2 | 2.3322×10^2 | 2.4363×10^2 | 2.4613×10^2 | 2.4674×10^2 |
| B_1 | 2.1495×10^{-2} | 2.1536×10^{-2} | 2.1545×10^{-2} | 2.1548×10^{-2} | 2.1548×10^{-2} |
| B_2 | 6.9688×10^{-2} | 6.7489×10^{-2} | 6.7015×10^{-2} | 6.6904×10^{-2} | 6.6877×10^{-2} |
| B_3 | 3.3585×10^{-3} | 3.0976×10^{-3} | 3.0423×10^{-3} | 3.0293×10^{-3} | 3.0262×10^{-3} |
| B_4 | 2.0421×10^{-2} | 1.7950×10^{-2} | 1.7454×10^{-2} | 1.7339×10^{-2} | 1.7311×10^{-2} |
| B_5 | 1.6990×10^{-3} | 1.3798×10^{-3} | 1.3181×10^{-3} | 1.3041×10^{-3} | 1.3007×10^{-3} |

Table 2 Dependence of $\bar{\lambda}_j$ and B_j , $j = 1, \dots, 5$, on the value of M_{SL} .

We now proceed by solving the full problem [IBVP] for a range of values of \hat{h} , and seeing how the values of $\text{meas}(\bar{M}')$, A_0^1 , $\bar{\lambda}_j$ and c_j , for $j = 1, 2, \dots$ are affected by the choice of \hat{h} , with all other parameters fixed (choosing in particular $L = 3$ and $M_{SL} = 100$). Computing times (cpt), number of nodes N_e and triangles N_t in the triangulation of the domain Ω , and our approximations to $\text{meas}(\bar{M}')$ and A_0^1 are shown in Table 3. All computations were carried out using Matlab on a desktop PC with an Intel(R) Core(TM2) Duo 2.66GHZ processor, with 1.96GB of RAM. We expect that faster computation times could be achieved with some optimization of the code. Our approximations to both $\text{meas}(\bar{M}')$ and A_0^1 appear to be converging as \hat{h} decreases.

In Table 4, we show our approximations to $\tilde{\lambda}_j$ and c_j , for $j = 1, \dots, 5$. Our approximations to $\tilde{\lambda}_j$ are converging as \hat{h} decreases, for each $j = 1, \dots, 5$. Our approximation to c_3 is also clearly converging as \hat{h} decreases, with all other values of c_j being very close to zero.

For the remainder of this section, we take the maximum triangle side length \hat{h} to be 0.01, and based on the results above we choose $L = 3$, $M_{SL} = 100$, and we consider the first five values of $\bar{\lambda}_j$ in the series expansion for the solution in the “inner” region, and the first fifteen values of $\tilde{\lambda}_j$ for the solution of the “transient” problem. These choices are motivated by the results in Tables 2 and 4, which show that the eigenvalues $\bar{\lambda}_j$ are growing very quickly as j increases, whereas the eigenvalues $\tilde{\lambda}_j$ are growing only slowly as j increases.

| | $\hat{h} = 0.16$ | $\hat{h} = 0.08$ | $\hat{h} = 0.04$ | $\hat{h} = 0.02$ | $\hat{h} = 0.01$ |
|--------------------|-------------------|-------------------|-------------------|-------------------|-------------------|
| cpt(s) | 3.9×10^0 | 5.4×10^0 | 1.5×10^1 | 5.5×10^1 | 2.6×10^2 |
| N_e | 69 | 281 | 1125 | 4527 | 18134 |
| N_t | 109 | 503 | 2128 | 8811 | 35779 |
| meas(\bar{M}') | 2.3148 | 2.3469 | 2.3540 | 2.3556 | 2.3561 |
| A_0^1 | 1.2398 | 1.2143 | 1.2037 | 1.1895 | 1.2036 |

Table 3 Computing times (in seconds), number of elements, and the dependence of meas(\bar{M}') and A_0^1 on \hat{h} .

| | $\hat{h} = 0.16$ | $\hat{h} = 0.08$ | $\hat{h} = 0.04$ | $\hat{h} = 0.02$ | $\hat{h} = 0.01$ |
|---------------------|--------------------------|---------------------------|--------------------------|--------------------------|--------------------------|
| $\tilde{\lambda}_1$ | $4.2460 \times 10^{+0}$ | $4.3161 \times 10^{+0}$ | $4.3299 \times 10^{+0}$ | $4.3335 \times 10^{+0}$ | $4.3341 \times 10^{+0}$ |
| $\tilde{\lambda}_2$ | $1.2714 \times 10^{+1}$ | $1.3199 \times 10^{+1}$ | $1.3303 \times 10^{+1}$ | $1.3327 \times 10^{+1}$ | $1.3332 \times 10^{+1}$ |
| $\tilde{\lambda}_3$ | $1.6001 \times 10^{+1}$ | $1.6560 \times 10^{+1}$ | $1.6674 \times 10^{+1}$ | $1.6701 \times 10^{+1}$ | $1.6707 \times 10^{+1}$ |
| $\tilde{\lambda}_4$ | $2.6131 \times 10^{+1}$ | $2.7720 \times 10^{+1}$ | $2.8050 \times 10^{+1}$ | $2.8131 \times 10^{+1}$ | $2.8151 \times 10^{+1}$ |
| $\tilde{\lambda}_5$ | $3.3527 \times 10^{+1}$ | $3.5453 \times 10^{+1}$ | $3.5840 \times 10^{+1}$ | $3.5931 \times 10^{+1}$ | $3.5951 \times 10^{+1}$ |
| c_1 | 5.1942×10^{-4} | 4.6234×10^{-11} | 4.6381×10^{-10} | 3.1984×10^{-8} | 1.7764×10^{-7} |
| c_2 | -2.0810×10^{-3} | -1.3308×10^{-4} | -1.3720×10^{-7} | -5.5753×10^{-7} | -2.1100×10^{-6} |
| c_3 | -4.3931×10^{-2} | -5.2523×10^{-2} | -5.5294×10^{-2} | -5.5673×10^{-2} | -5.5845×10^{-2} |
| c_4 | 7.3635×10^{-4} | 9.3427×10^{-11} | 4.0908×10^{-9} | 6.1409×10^{-9} | 1.1863×10^{-7} |
| c_5 | -1.2053×10^{-3} | -2.4342×10^{-11} | -5.4567×10^{-9} | -2.7396×10^{-9} | -7.2959×10^{-8} |

Table 4 Dependence of $\tilde{\lambda}_j$ and c_j on \hat{h} , for $j = 1, 2, \dots$

We remark that further tests were carried out above and beyond those reported here, in order to convince ourselves that these parameter choices were sensible.

A plot of $A(x, y) \approx \hat{p}(x, y, z; \epsilon)$ (recall (3.9)) solving [BVP] is shown in Figure 1(a). The radial symmetry of $A(x, y)$ around the source at $(0, 0)$ can be clearly seen, as predicted by (2.45). In Figure 2(a) we plot $A(x, 0)$ and also

$$\frac{-\alpha_1}{4\pi(\bar{D}_x\bar{D}_y)^{\frac{1}{2}}} \log \left[\frac{(x-x_1)^2}{\bar{D}_x} + \frac{(y-y_1)^2}{\bar{D}_y} \right] = \frac{1}{4\pi} \log(x^2),$$

for $x \in (0, 1)$. Equation (2.45) suggests that we should expect to see

$$A(x, 0) = \frac{1}{4\pi} \log(x^2) + A_0^1 + O(x), \quad \text{as } x \rightarrow 0. \quad (4.2)$$

From Figure 2(a) this seems plausible, with both plots exhibiting similar behaviour, separated by a roughly constant value. To test (4.2) more carefully, in Figure 2(b) we plot $A(x, 0) - \log(x^2)/(4\pi)$. If (4.2) is correct, we would expect to see a linear plot; this certainly appears to be the case, suggesting that the behaviour predicted by (2.45) is being attained numerically. For comparative purposes, in Figure 2(b) we also plot $-0.1633x + 1.2089$, the best fitting least squares linear approximation to $A(x, 0) - \log(x^2)/(4\pi)$. The line is clearly

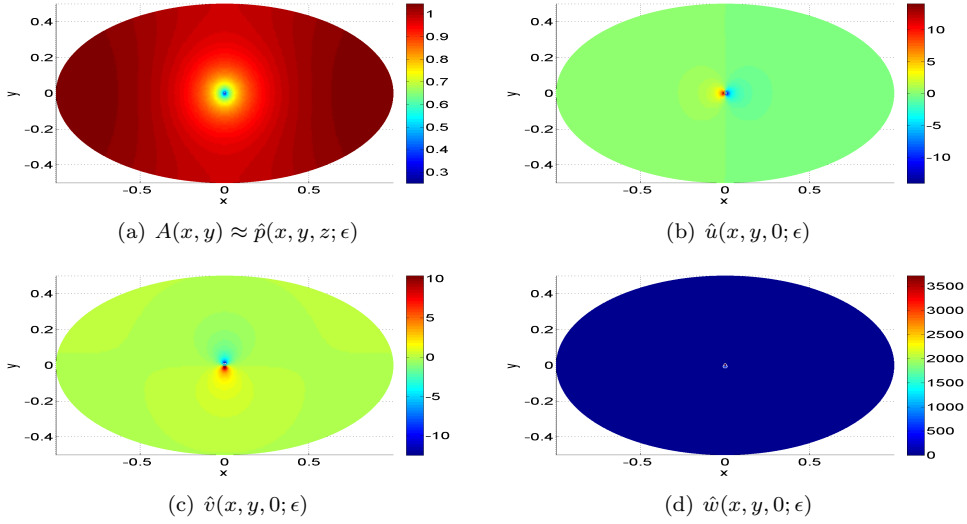


Fig. 1 Outer region pseudo-steady state pressure and flow fields, Example 4.1.

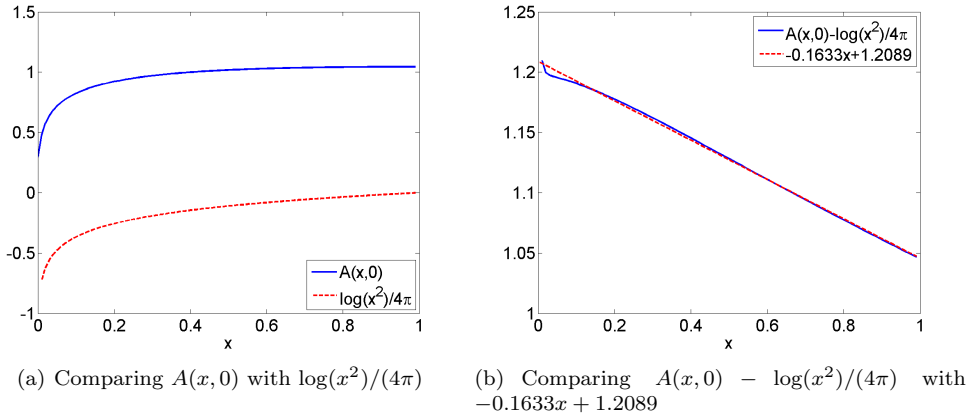


Fig. 2 Verifying equation (2.45).

a very good fit to the data, suggesting a value of the constant $A_0^1 \approx 1.2089$ in (4.2). This compares well with the value of $A_0^1 = 1.2036$ given in Table 3, which was computed using a similar approach in all four coordinate directions, but only sampling at five points in each of those directions, as described in §3.3.

Having plotted $A(x, y)$, the leading order approximation to the pseudo-steady state pressure field \hat{p} in the “outer” region, in Figure 1(a), we also plot in Figures 1(b)–(d) the leading order approximations to the pseudo-steady state flow fields in the x -direction,

\hat{u} , the y -direction, \hat{v} , and the z -direction, \hat{w} , each on a slice through \overline{M}' on the plane $z = 0$. The plots of $\hat{u}(x, y, 0; \epsilon)$ and $\hat{v}(x, y, 0; \epsilon)$, in Figures 1(b) and 1(c) respectively, demonstrate how the flow fields in the x and y directions are highly peaked near the line sink, and the dependence on the derivatives of $A(x, y)$ as plotted in Figure 1(a) is clear. The plot of $\hat{w}(x, y, 0; \epsilon)$ in Figure 1(d) shows that the flow is almost entirely horizontal away from the wells, with the flow field in the vertical direction being very highly peaked at the line sink.

In Figure 3 we plot the pseudo-steady state pressure and flow fields in the inner regions. Each of these is computed at a distance $\epsilon/100$ from the line sink, at the point $x = y = \epsilon/(100\sqrt{2})$, and then plotted as a function of z , the vertical coordinate. At this very small

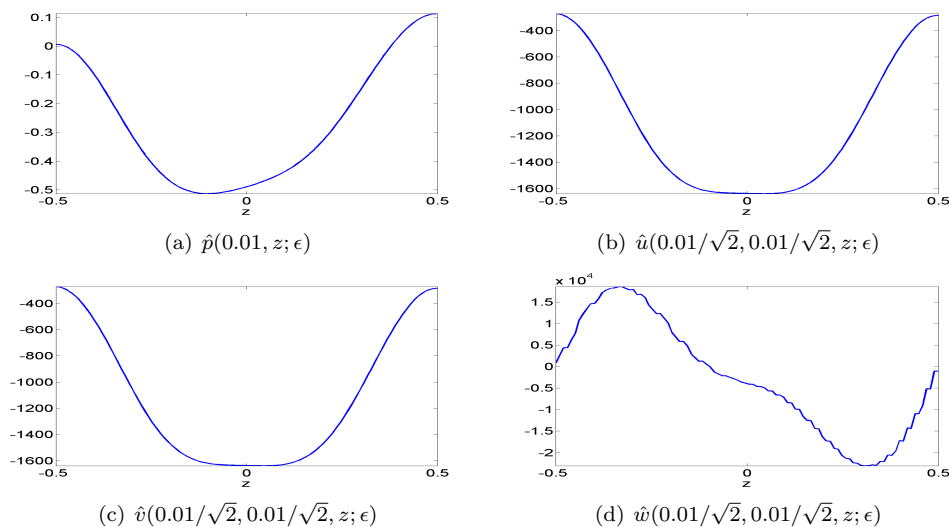


Fig. 3 Inner region pseudo-steady state pressure and flow fields.

distance from the line sink, the pseudo-steady state pressure field and the pseudo-steady state flow fields in the x and y directions each take their largest absolute values near the centre of the layer. The pseudo-steady state flow field in the z -direction is close to zero at the upper and lower boundaries, as we would expect from the Neumann boundary conditions, but the vertical flow field is also close to zero near the centre of the layer, positive in the lower part of the layer, and negative in the upper part of the layer, indicating that the fluid is flowing towards the centre of the layer at all points near the line sink. We remark that the approximation to \hat{w} is piecewise constant, and at the level of graphical magnification this is evident in Figure 3(d).

We plot our approximation to the transient pressure field $\tilde{p}(\mathbf{r}, t)$ for $t = 1/400$ and $t = 0.1$ in Figure 4. Recalling (2.59), we note that our approximation to \tilde{p} is only valid when $t \gg \epsilon^2 = 1/10000$. Examining the scales on the right of each of these figures, the decay of the transient pressure field with respect to time is clear (recall (2.34) and (2.36)). Further plots for larger values of t look identical to Figure 4(b), but with $|\tilde{p}(\mathbf{r}, t)|$ decreasing (apparently uniformly) as t increases. Although the early time solution is peaked near the line sink, it

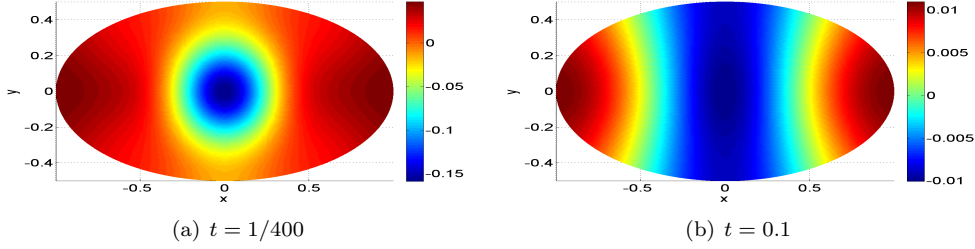


Fig. 4 Transient pressure field, $\tilde{p}(\mathbf{r}, t)$, computed at $t = 1/400$ and $t = 0.1$, Example 4.1.

is smooth at this point, with the singularity being captured entirely by the pseudo-steady state solution, and the evolutionary problem providing a smooth solution.

The transient flow fields in the x and y directions, $\tilde{u}(\mathbf{r}, t)$ and $\tilde{v}(\mathbf{r}, t)$ respectively, defined by (2.33) and computed at $t = 1/400$, are plotted on a slice through $z = 0$ in Figure 5. The

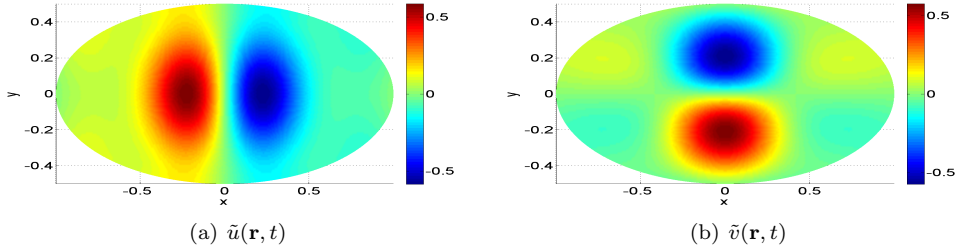


Fig. 5 Transient flow fields in x - and y -directions, computed at $t = 1/400$, $z = 0$, Example 4.1.

relationship between these flow fields and the corresponding transient pressure field plotted in Figure 4(a) can be clearly seen.

EXAMPLE 4.2 (Change in strength of line sources/sinks). For our second example, we consider the effect of changing the strength of the single line source/sink located at $(x_1, y_1) = (0, 0)$, keeping everything else the same. In order to model a change in the line source/sink volumetric strengths, there is no need to repeat all of the calculations, particularly if the line source/sink locations are not changed. In this case we just redefine s_i , for $i = 1, \dots, N$, and then solve [IBVP] for these new line source/sink strengths, taking the final solution from the previous run as our initial data. Here, we take our initial data to be the solution from Example 4.1 at $t = 0.2$, and we halve the strength of the sink at $(x_1, y_1) = (0, 0)$ (given by (4.1) for Example 4.1), so that now

$$s_1(z) = -3(z_+^1 - z)(z - z_-^1).$$

This corresponds to halving the production rate at the well. In Figure 6 we plot the

dimensional dynamic fluid pressure,

$$p(x, y, 0, t') = Q\bar{p}(x, y, 0, t) \quad (4.3)$$

(see (6, §2) for details, recalling that Q is given by (2.9)), computed at a dimensionless distance $\epsilon/100$ from the line sink, as for the computations of Figure 3 above, against dimensional time ($t' = 5000t$, again see (6, §2) for details) with the line sink strength having been halved at $t = 0.2$, corresponding to $t' = 1000$. Looking first at the solution for

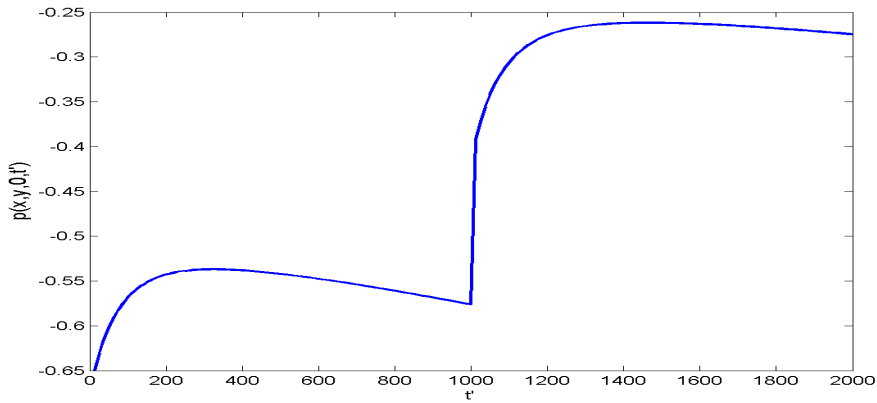


Fig. 6 Dimensional dynamic fluid pressure (computed at a dimensionless distance $\epsilon/100$ from the line sink) plotted against dimensional time, with the production rate being halved at $t' = 1000$.

$t' \in (0, 1000)$, the initial effect of the transient field is clear. By about $t' = 300$ this has been overtaken by the linear decay in the pressure, due to the fact that $\hat{\alpha}_T$, corresponding to the sum of the volume fluxes from the line sources/sinks (recall (2.20)), is negative. At $t' = 1000$, we see the effect of the change in production rate. The computing time required to approximate the dynamic fluid pressure for $t' \in (1000, 2000)$ is only 64 seconds, compared to a computing time of 260 seconds for Example 4.1 (both values correct to two significant figures). This reduced computing time is due to the fact that many of the calculations from the original run do not need to be repeated; once an initial overhead cost is taken into account, changes to production rates can be computed very quickly. We repeat our earlier comment that we expect that these computation times could be reduced further with some optimization of the code.

EXAMPLE 4.3 (Change in number, locations and strengths of line sources/sinks). In addition to changing the volumetric strengths of the line sources/sinks, it is also straightforward to compute the solution to [IBVP] for a completely new configuration of line sources/sinks, with strengths that may or may not be the same as those of the previous ones. In this case, the computational time will again be significantly less than for the original run, as there is no need to regenerate the mesh on Ω , nor to recompute those parts of the solution that are independent of the location and strengths of the line sources/sinks. For example, the

stiffness matrix for the solution of both [BVP] and [EVP]' is unaffected by changes to the strengths/locations of the sources/sinks. As a third example, we consider the case of three line sources/sinks, located at $(x_1, y_1) = (-0.5, 0)$, $(x_2, y_2) = (0.5, 0)$ and $(x_3, y_3) = (0, 0.1)$, with volumetric strengths

$$\begin{aligned} s_1(z) &= 3.5(z_+^1 - z)(z - z_-^1), \\ s_2(z) &= 2.5(z_+^2 - z)(z - z_-^2), \\ s_3(z) &= -3(z_+^3 - z)(z - z_-^3), \end{aligned}$$

respectively. Everything else in this example is identical to Examples 4.1 and 4.2. The total computing time for solving [IBVP] for this new configuration of line sources/sinks (reusing some calculations from Example 4.1) is only 150 seconds, again compared with a computing time of 260 seconds for the (simpler) Example 4.1. For this new example with three line sources/sinks, we plot figures comparable to those for Example 4.1, in order to demonstrate how our approach can cope very easily with more complicated line source/sink configurations.

Plots of $A(x, y) \approx \hat{p}(x, y, z; \epsilon)$, $\hat{u}(x, y, z; \epsilon)$, $\hat{v}(x, y, z; \epsilon)$ and $\hat{w}(x, y, z; \epsilon)$ are shown in Figure 7. The radial symmetry of $A(x, y)$ around each of the three line source/sinks can be

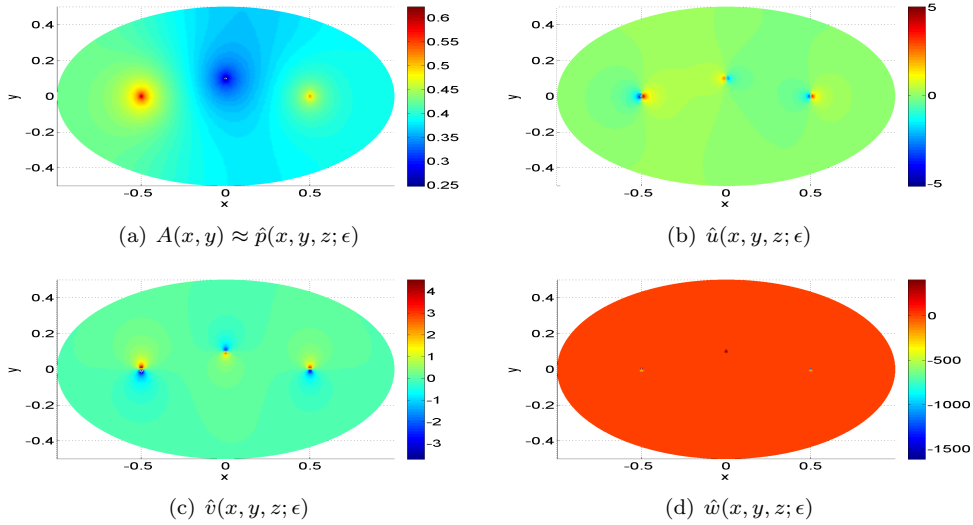


Fig. 7 Outer region pseudo-steady state pressure and flow fields, Example 4.3.

clearly seen, as predicted by (2.45). The plots of $\hat{u}(x, y, 0, \epsilon)$ and $\hat{v}(x, y, 0, \epsilon)$, in Figures 7(b) and 7(c) respectively, again demonstrate how the flow fields in the x and y directions are highly peaked near the line sources/sinks, and the dependence on the derivatives of $A(x, y)$ as plotted in Figure 7(a) is again clear. The plot of $\hat{w}(x, y, 0, \epsilon)$ in Figure 7(d) shows how the flow is almost entirely horizontal away from the wells, even with several line sources/sinks, with the flow field in the vertical direction being very highly peaked at the line sources/sinks.

In Figure 8 we plot the pseudo-steady state pressure and flow fields in the inner regions around each line source/sink. Each of these is computed at a distance $\epsilon/100$ from each line sink, at the point $(x - x_i) = (y - y_i) = \epsilon/(100\sqrt{2})$, for $i = 1, 2, 3$, and plotted as a function of z , the vertical coordinate. The behaviour near each line source/sink is comparable to

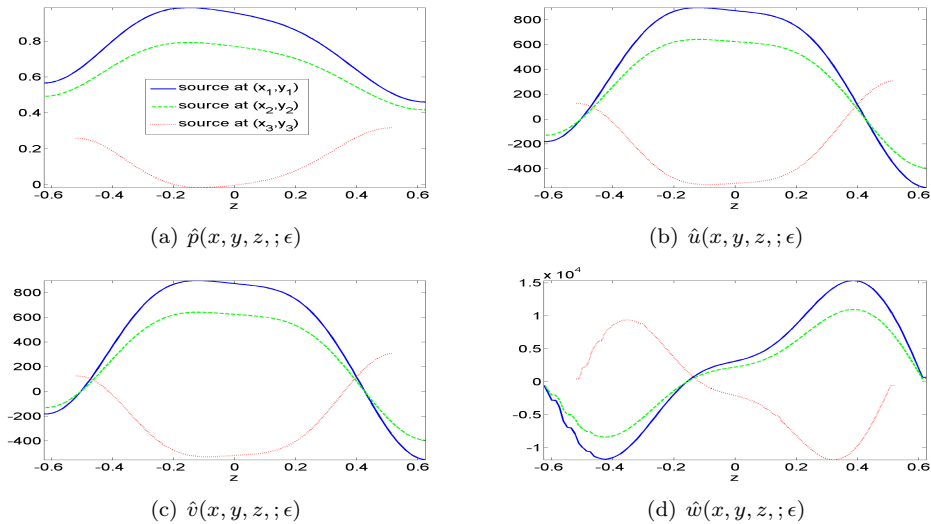


Fig. 8 Inner region pseudo-steady state pressure and flow fields, each computed at a distance $\epsilon/100$ from each source/sink. The legend is the same for each plot.

that seen in Figure 3 for Example 4.1. For the sink at $(x_3, y_3) = (0, 0.1)$, the vertical flow field is positive in the lower part of the layer, and negative in the upper part of the layer, indicating that the fluid is flowing towards the centre of the layer at all points near the line sink. For each of the sources, the vertical flow field is negative in the lower part of the layer, and positive in the upper part of the layer, indicating that the fluid is flowing away from the centre of the layer at all points near the line sources.

We plot our approximation to the transient pressure field $\tilde{p}(\mathbf{r}, t)$ for $t = 1/400$, $t = 0.05$, $t = 0.1$ and $t = 0.2$ in Figure 9. Examining the scales on the right of each of these plots, the decay of the transient pressure field with respect to time is again clear. This decay is much slower than for Example 4.1 (compare with Figure 4). The transient flow fields in the x and y directions, $\tilde{u}(\mathbf{r}, t)$ and $\tilde{v}(\mathbf{r}, t)$ respectively, defined by (2.33) and computed at $t = 1/400$, are plotted on a slice through $z = 0$ in Figure 10. The relationship between these flow fields and the corresponding transient pressure field plotted in Figure 9(a) is clear.

We conclude this example with a plot (Figure 11) showing how the dimensional pressure, again given in this case by (4.3) and computed at a dimensionless distance $\epsilon/100$ from the line sources/sinks (as for the computations of Figure 8 above), varies with respect to dimensional time. The initial effect of the transient field can clearly be seen near each line source/sink. By about $t' = 200$ this has been overtaken by the linear increase in the

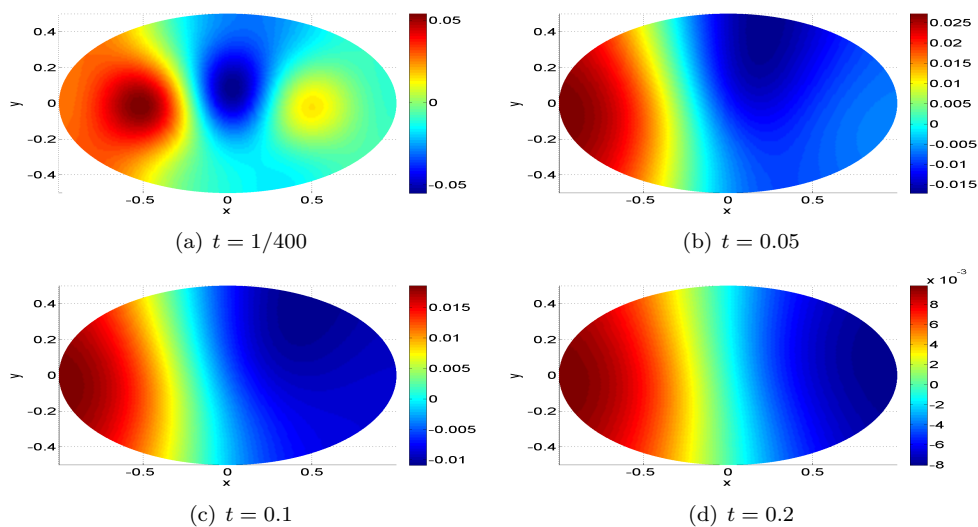


Fig. 9 Transient pressure field, $\tilde{p}(\mathbf{r}, t)$, computed for various t , Example 4.3.

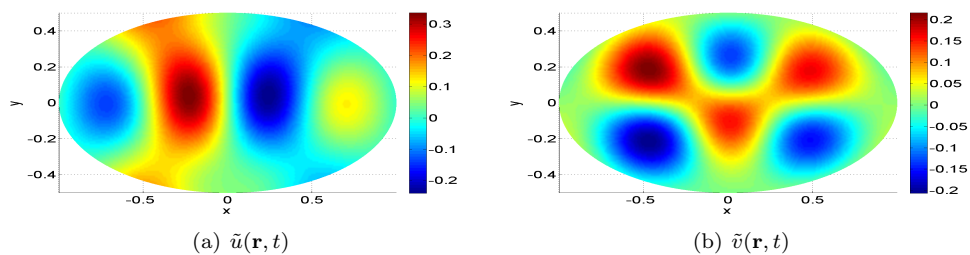


Fig. 10 Transient flow fields in x - and y -directions, computed at $t = 1/400$, $z = 0$, Example 4.3.

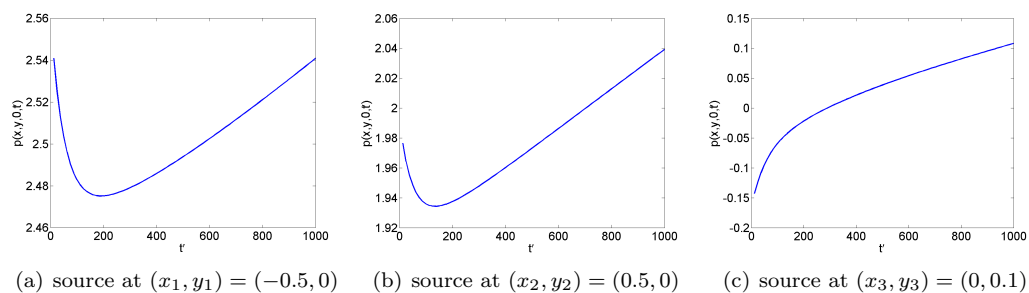


Fig. 11 Dimensional pressure plotted against dimensional time, computed at a dimensionless distance $\epsilon/100$ from each line source, Example 4.3.

pressure, due to the fact that $\hat{\alpha}_T$, corresponding to the sum of the volume fluxes from the line sources/sinks, is positive.

EXAMPLE 4.4 (Nonuniform porosity). Finally we remark that having solved [IBVP] once, one can change certain properties of the porous layer, such as its porosity or permeability, and then recompute the solution to [IBVP] with a greatly reduced computing time, with no need to repeat calculations that are not explicitly dependent on the changed feature. To illustrate this, for our final example, we change the porosity function so that it is no longer constant, but instead is defined by $\bar{\phi} = \Phi(x, y, z)/\Phi_0$, where

$$\Phi(x, y, z) = 0.5 + 0.4 \sin \left(2\pi \left(\frac{z - z_-(x, y)}{z_+(x, y) - z_-(x, y)} \right) \right),$$

and

$$\Phi_0 = \frac{1}{\text{meas}(\bar{M}')} \iiint_{\bar{M}'} \Phi(x, y, z) \, dx \, dy \, dz,$$

so that (2.7) holds. This models a porosity function that varies with depth, as one might find in a smoothly varying layered media. Having solved [IBVP] for Example 4.3, we then recompute the solution for the new porosity function. The computing time for this final run is 130 seconds, half of the computing time of 260 seconds required to solve Example 4.1 from scratch.

For this final example with nonuniform porosity, we plot in Figure 12 the dimensional pressure (again given by (4.3)) at a dimensionless distance $\epsilon/100$ from the line sources/sinks (as for the other examples above) against dimensional time. Again, the initial effect of the

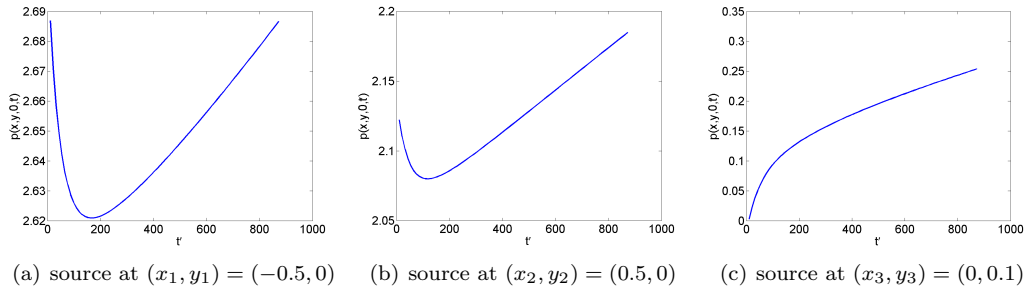


Fig. 12 Dimensional pressure plotted against dimensional time, computed at a dimensionless distance $\epsilon/100$ from each source, Example 4.4.

transient field can clearly be seen near each line source/sink. By about $t' = 200$ this has been overtaken by the linear increase in the pressure, due to the fact that $\hat{\alpha}_T$, corresponding to the sum of the volume fluxes from the line sources/sinks, is positive. Note that the dimensional time scale here is different from before, even though each of our examples is considered over the same dimensionless time interval. This is due to the variation in Φ_0 here, which has an effect on the scaling; for details, we refer to (6, §2). We finally remark that plots of the pseudo-steady state pressure and flow fields and of the transient pressure

and flow fields, comparable to Figures 7–10, look qualitatively the same as for Example 4.3, and so we do not plot any further figures here.

5. Conclusions

In this paper we have considered the unsteady flow of a weakly compressible fluid in a horizontal layer of an inhomogeneous and anisotropic porous medium with variable upper and lower boundaries, in the presence of vertical line sources and sinks. We have described, algorithmically, how to construct the solution to a strongly parabolic linear initial-boundary value problem for the dynamic fluid pressure, when the layer aspect ratio $0 < \epsilon \ll 1$, via the method of matched asymptotic expansions. This approach leads to several problems that must be solved numerically: a linear, inhomogeneous, strongly elliptic 2-d boundary value problem, a 2-d regular self-adjoint eigenvalue problem, and a 1-d regular Sturm-Liouville eigenvalue problem. We have described explicitly how to solve these problems individually, and how to put all of the numerical solutions together in order to describe the solution to the full 3-d initial-boundary value problem throughout the reservoir, providing a full description of the entire computational procedure required to obtain numerical approximations to the pressure and flow fields.

Examples demonstrating the application of the theory to some simple situations are provided. In particular, we note that on a desktop PC one can solve the full 3-d initial-boundary value problem in computing times that are measured in seconds rather than hours. Moreover, once an initial computational overhead has been accounted for, altered versions of the initial-boundary value problem with different porosity or permeability functions, or different well locations, can be solved in a fraction of the time required for the initial solve. The ease with which one can change source/sink strengths and locations within the framework of our method makes this approach well suited to determining optimal well locations, for example, and the ease with which the porosity and permeability functions can be changed may make the ideas developed here attractive in applications such as history matching, for example using measurements of the pressure and/or flow fields near the wells in order to determine the porosity throughout the layer. Finally, we remark that many of the formulations arising in this approach that involve geological features such as permeability and porosity of the inhomogeneous media require only the depth integrated values of these quantities, thereby potentially reducing the impact of uncertain data.

References

1. R. E. Ewing, G. Qin, and W. Zhao. High performance computing in petroleum applications. *Int. J. Numer. Anal. Model.*, 2:43–57, 2005.
2. Z. Chen. *Reservoir Simulation: Mathematical Techniques in Oil Recovery*. SIAM, 2007.
3. H. Wang, W. Zhao, R. E. Ewing, M. Al-Lawatia, M. Espedal, and A. S. Telyakovskiy. An Eulerian-Lagrangian solution technique for single-phase compositional flow in three-dimensional porous media. *Comput. Math. Appl.*, 52:607–624, 2006.
4. F. O. Alpak, C. Torres-Verdín, K. Sepehrnoori, S. Fang, and L. Knizhnerman. An extended Krylov subspace method to simulate single-phase fluid flow phenomena in axisymmetric and anisotropic porous media. *Journal of Petroleum Science and Engineering*, 40:121–144, 2003.
5. D. J. Needham, S. Langdon, G. S. Busswell, and J. P. Gilchrist. The unsteady flow of

- a weakly compressible fluid in a thin porous layer. I: Two-dimensional theory. *SIAM J. Appl. Math.*, 69(4):1084–1109, 2009.
6. D. J. Needham, S. Langdon, B. A. Samson, and J. P. Gilchrist. The unsteady flow of a weakly compressible fluid in a thin porous layer. II: Three-dimensional theory. Submitted for publication, University of Reading preprint MPS-2011-02, 2011.
 7. V. Isakov. On inverse problems in secondary oil recovery. *European J. Appl. Math.*, 19:459–478, 2008.
 8. O. Dorn and R. Villegas. History matching of petroleum reservoirs using a level set technique. *Inverse Problems*, 24(3):035015, 2008.
 9. A. Friedman. *Partial Differential Equations of Parabolic Type*. Prentice-Hall, Englewood Cliffs, N.J., 1964.
 10. M. Abramowitz and I. Stegun. *Handbook of Mathematical Functions*. Dover, 1972.
 11. E. A. Coddington and N. Levinson. *Theory of Ordinary Differential Equations*. McGraw-Hill Book Company, Inc., New York-Toronto-London, 1955.
 12. J. Smoller. *Shock Waves and Reaction-Diffusion Equations*. Springer-Verlag, Berlin, 1983.
 13. G. Strang and G. J. Fix. *An Analysis of the Finite Element Method*. Prentice-Hall, Inc., Englewood Cliffs, N.J., 1973.
 14. O. C. Zienkiewicz and K. Morgan. *Finite Elements and Approximation*. John Wiley and Sons, Inc., 1983.
 15. P.-O. Persson and G. Strang. A simple mesh generator in MATLAB. *SIAM Review*, 46:329–345, 2004.
 16. D. Braess. *Finite Elements: Theory, Fast Solvers, and Applications in Solid Mechanics*. Cambridge University Press, 1997.
 17. J. W. Barrett and C. M. Elliott. A practical finite element approximation of a semi-definite Neumann problem on a curved domain. *Numer. Math.*, 51:23–36, 1987.
 18. H. S. Dollar. Constraint-style preconditioners for regularized saddle point problems. *SIAM J. Matrix Anal. Appl.*, 29(2):672–684, 2007.
 19. D. Huybrechs and R. Cools. On generalized Gaussian quadrature rules for singular and nearly singular integrals. *SIAM J. Numer. Anal.*, 47(1):719–739, 2008.
 20. C. Schwab. Variable order composite quadrature of singular and nearly singular integrals. *Computing*, 53:173–194, 1994.